

**DEVELOPMENT OF ZIRCONIA NANOTUBES  
AND IRON OXIDE NANOPORES BY  
ANODIZATION METHOD FOR PHOTOACTIVE  
MATERIAL**

**MONNA ROZANA**

**UNIVERSITI SAINS MALAYSIA**

**2018**

**DEVELOPMENT OF ZIRCONIA NANOTUBES  
AND IRON OXIDE NANOPORES BY ANODIZATION METHOD  
FOR PHOTOACTIVE MATERIAL**

**by**

**MONNA ROZANA**

**Thesis submitted in fulfillment of the  
requirements for the degree of  
Doctor of Philosophy**

**May 2018**

## DECLARATION

I hereby declare that I have conducted, completed the research work and written the thesis entitles “Development of Zirconia Nanotubes and Iron Oxide Nanopores by Anodization Method for Photoactive Material”. I also declare that it has not been previously submitted for the award of any degree or diploma or other similar title of this for any other examining body or university.

Name of Student: Monna Rozana

Signature:

Date: 4 May 2018

Witness by

Supervisor: Assoc. Prof. Dr. Zainovia Lockman

Signature:

Date: 4 May 2018

## ACKNOWLEDGEMENT

In the name of ALLAH, the Most Gracious and the Most Merciful.

Alhamdulillah, all praises to ALLAH for the strengths and His blessing in completing this study. Nothing happens except in accordance with ALLAH's will.

First of all, I would like to express my most sincere gratitude to my supervisor, Assoc. Prof. Dr. Zainovia Lockman for her patience, guidance and perpetual encouragement throughout my doctoral study. It would not have been possible for me to complete this thesis without her help and constant support. I am indebted to her for introducing me to materials science and giving me an opportunity to work on nanomaterials. I really admire her in so many ways.

I also would like to thank Prof. Atsunori Matsuda from Toyohashi University of Technology (TUT) for his guidance, Dr. Go Kawamura and Dr. Tan Wai Kian for their help during my attachment at TUT, Dr. Teruhisa Okuno, Dr. Nguyen Huu Huy Phuc and Adrian Ashari for their kindly help to guide me on operating various material characterization machines.

I am deeply thankful to School of Materials and Mineral Resources Engineering, Universiti Sains Malaysia (USM) for offering an opportunity to pursue doctoral degree with great supports from academic, technical, and administrative staffs. I am grateful to ASEAN University Network/Southeast Asia Engineering Education Development Network (AUN/SEED-Net) and Japan International Cooperation Agency (JICA) for financial support and great opportunity for collaborative research with TUT. My sincere gratitude goes to Long Term Research Grant Scheme (LRGS) under OneBAJA project from Ministry of Higher Education Malaysia for partially support laboratory expenses for this research work.

Many people have highlighted my life experience in USM and deserve mentioning. I benefited greatly from the intellectual interaction with Assoc. Prof. Dr. Syafrudin Masri and his wife, Dr. Adhi Kusumastuti and her husband, Madam Fong, Encik Mohd Azzam Rejab, Puan Haslina Zulkifli, Encik Kemuridan Md. Desa and Encik Mohammad Azrul Zainol Abidin. I thank Encik Abdul Rashid Selamat and Encik Muhammad Khairi Khalid for their kindly help to train me on operating Scanning Electron Microscope. I also thank for social interactions to my colleagues at Electronics Lab and GEMS group, particularly to Mustaffa Ali Azhar Taib, Nurhaswani Alias, Nurul Izza Soaid and Nurul Nadia Mohd Zorkipli. Not forget to Dr. Muhammad Syukron, Dr. Khairul Arifah Saharudin, Ervina Junaidi, Nor Azlina Ahmad and Chow Yuh Nien. Their friendship is a blessing.

Finally, I would like to express special gratitude to my beloved parents; Erniwati, S.H and Iroza for their pray and unconditional love. It is impossible for me to finish this doctoral study without their support financially and morally. I also thank my sister; Chichi Rosalinda, S.E., M.M. and her kids for their love. Last but not least, to everybody who painted the story in accomplishment of this study successfully, thank you.

Monna Rozana

4 May 2018

## TABLE OF CONTENTS

	Page
<b>ACKNOWLEDGEMENT</b>	ii
<b>TABLE OF CONTENTS</b>	iv
<b>LIST OF TABLES</b>	viii
<b>LIST OF FIGURES</b>	xi
<b>LIST OF ABBREVIATIONS</b>	xxiii
<b>LIST OF SYMBOLS</b>	xxv
<b>ABSTRAK</b>	xxvii
<b>ABSTRACT</b>	xxix

### CHAPTER ONE : INTRODUCTION

1.1	Background	1
	1.1.1 Electricity generation	1
	1.1.2 Dye pollution in water	4
1.2	Photoactive material	6
1.3	Synthesis method of nanostructured ZrO <sub>2</sub> and $\alpha$ -Fe <sub>2</sub> O <sub>3</sub>	10
1.4	Problem statements	12
1.5	Research objectives	17
1.6	Research scope	17
1.7	Thesis outline	18

### CHAPTER TWO : LITERATURE REVIEW

2.1	Introduction	19
2.2	Anodization process for nanostructuring	19
2.3	Anodization of Zr metal for ZNTs formation	24
	2.3.1 Progress in Zr metal anodization in various types of electrolyte	24
	2.3.2 Growth mechanism model of ZNTs	33
	2.3.3 Factors affecting the growth of ZNTs	39

2.3.4	Methods to form FS-ZNTs	45
2.3.5	Crystallinity of ZNTs	47
	2.3.5(a) Phases of ZrO <sub>2</sub> and its stabilization at room temperature	47
	2.3.5(b) Crystallinity of as-anodized and annealed anodic ZrO <sub>2</sub>	52
2.3.6	Properties of ZNTs	56
2.3.7	Photoactivity of ZNTs	61
2.4	Anodization of Fe metal for FNPs and FNTs formation	66
2.4.1	Anodization of Fe in various electrolyte	66
2.4.2	Crystallinity of FNPs and FNTs	70
	2.4.2(a) Phases of iron oxides	71
	2.4.2(b) Crystallinity of as-anodized and annealed FNPs and FNTs	73
2.4.3	Photoactivity of $\alpha$ -Fe <sub>2</sub> O <sub>3</sub>	76

### **CHAPTER THREE : METHODOLOGY**

3.1	Introduction	81
3.2	Raw materials and chemical selection	81
3.3	Experimental procedure	85
	3.3.1 Sample preparation	86
	3.3.2 Electrolyte preparation	86
	3.3.3 Anodization	87
	3.3.3(a) Anodization of Zr	89
	3.3.3(b) Anodization of Fe	91
	3.3.4 Cleaning of as-anodized foil	92
	3.3.5 Annealing	92
	3.3.6 Photocurrent measurement	93
	3.3.7 MO degradation	95
3.4	Characterization	96
	3.4.1 Morphology	96
	3.4.2 Crystallinity	98

3.4.3	Surface composition	101
3.4.4	Optical property	101
3.4.5	Surface area	103

## CHAPTER FOUR : RESULTS AND DISCUSSION

4.1	Introduction	104
4.2	Anodization of Zr in NH <sub>4</sub> F/EG electrolyte	104
4.3	Anodization of Zr in H <sub>2</sub> O/NH <sub>4</sub> F/EG electrolyte	107
4.4	Anodization of Zr in KOH/NH <sub>4</sub> F/EG electrolyte	117
4.4.1	Effect of KOH content in NH <sub>4</sub> F/EG electrolyte	118
4.4.2	Effect of KOH molarity in NH <sub>4</sub> F/EG electrolyte	124
4.4.3	Effect of applied voltage on KOH/NH <sub>4</sub> F/EG electrolyte	129
4.4.4	Effect of annealing temperature	135
4.5	Anodization of Zr in LiOH/NH <sub>4</sub> F/EG electrolyte	141
4.5.1	Effect of LiOH molarity in NH <sub>4</sub> F/EG electrolyte	141
4.5.2	Effect of applied voltage in LiOH/NH <sub>4</sub> F/EG electrolyte	145
4.5.3	Effect of annealing temperature	153
4.6	Anodization of Zr in H <sub>2</sub> O <sub>2</sub> /NH <sub>4</sub> F/EG electrolyte	160
4.6.1	The metal oxide interface comparison of with and without H <sub>2</sub> O <sub>2</sub> addition into EG electrolyte	161
4.6.2	Effect of applied voltage in H <sub>2</sub> O <sub>2</sub> /NH <sub>4</sub> F/EG electrolyte	163
4.6.3	Effect of annealing temperatures to the phase transformation of FS-ZNTs	171
4.7	Photoactivity performance of ZNTs formed in H <sub>2</sub> O, KOH, LiOH, and H <sub>2</sub> O <sub>2</sub> added NH <sub>4</sub> F/EG electrolyte	180
4.8	Anodization of Fe in H <sub>2</sub> O, KOH, LiOH and H <sub>2</sub> O <sub>2</sub> added NH <sub>4</sub> F/EG electrolyte	194
4.8.1	Anodization of Fe in H <sub>2</sub> O/NH <sub>4</sub> F/EG electrolyte	194
4.8.2	Anodization of Fe in KOH/NH <sub>4</sub> F/EG electrolyte	206
4.8.3	Anodization of Fe in LiOH/NH <sub>4</sub> F/EG electrolyte	216



4.8.4	Anodization of Fe in H <sub>2</sub> O <sub>2</sub> /NH <sub>4</sub> F/EG electrolyte	224
4.8.5	Photoactivity performance of FNPs or FNTs formed in H <sub>2</sub> O, KOH, LiOH and H <sub>2</sub> O <sub>2</sub> added NH <sub>4</sub> F/EG electrolyte	232

## **CHAPTER FIVE : CONCLUSION AND RECOMMENDATIONS**

5.1	Conclusion	243
5.2	Recommendations	246

<b>REFERENCES</b>	<b>248</b>
-------------------	------------

## **LIST OF PUBLICATIONS**

## LIST OF TABLES

		Page
Table 1.1	Key indicators for Malaysia (IEA, 2015).	2
Table 1.2	Solar intensity in Malaysia (Mekhilef <i>et al.</i> , 2012).	3
Table 2.1	The development of ZNTs in ethylene glycol electrolyte.	30
Table 2.2	The evolution of anodic ZNTs.	31
Table 2.3	Methods to obtain FS-ZNTs.	46
Table 2.4	MO degradation on ZNTs from the literature.	65
Table 2.5	Types of morphology of anodic film on Fe substrate.	67
Table 2.6	The anodizing electrolyte and applied voltage for anodization of Fe to produce nanostructured anodic film on Fe.	69
Table 2.7	Comparison of photocurrent of nanostructured anodic $\alpha$ -Fe <sub>2</sub> O <sub>3</sub> photoanode.	79
Table 3.1	Thickness and purity of metal foils used for anodization.	81
Table 3.2	Chemical used for the anodization.	84
Table 3.3	Area of metal immersion into electrolyte.	88
Table 3.4	The parameter investigated on anodization of Zr.	90
Table 3.5	The parameter investigated on anodization of Fe.	92
Table 4.1	The pH and conductivity of EG electrolyte containing 0.27 wt.% NH <sub>4</sub> F and << 100 $\mu$ L H <sub>2</sub> O (measured at 25.5 °C).	108
Table 4.2	Excitation and emission spectra and corresponding photon energy for ZNTs annealed at 400 °C.	116
Table 4.3	The pH of EG electrolyte containing 0.27 wt.% NH <sub>4</sub> F and various amount of 1.0 M KOH (measured at 25.5 °C).	119
Table 4.4	Percentage of monoclinic and tetragonal ZrO <sub>2</sub> in ZNTs formed in different KOH content. ZNTs were	124

annealed at 400 °C for 2 h in air.

Table 4.5	Properties of EG electrolyte containing 0.27 wt.% NH <sub>4</sub> F and 3 mL of 0.5 – 3.0 M KOH	125
Table 4.6	Effect of KOH molarity in KOH/NH <sub>4</sub> F/EG electrolyte to the structural characteristics of ZNTs.	127
Table 4.7	Percentage of monoclinic and tetragonal ZrO <sub>2</sub> in ZNTs formed in different molarity of KOH. ZNTs were annealed at 400 °C for 2 h in air.	128
Table 4.8	Percentage of monoclinic and tetragonal ZrO <sub>2</sub> in ZNTs formed in different applied voltage in KOH/NH <sub>4</sub> F/EG electrolyte. ZNTs were annealed at 450 °C for 2 h in air.	134
Table 4.9	Percentage of monoclinic and tetragonal ZrO <sub>2</sub> in ZNTs formed in KOH/NH <sub>4</sub> F/EG electrolyte and annealed at various temperature for 2 h in air.	137
Table 4.10	Percentage of atomic concentration in ZNTs formed in KOH/NH <sub>4</sub> F/EG electrolyte and annealed at 400 °C.	139
Table 4.11	Properties of EG electrolyte containing 0.27 wt.% NH <sub>4</sub> F and 1 mL of 0.5 – 3.0 M LiOH.	142
Table 4.12	Percentage of monoclinic and tetragonal ZrO <sub>2</sub> in ZNTs formed in various applied voltage in LiOH/NH <sub>4</sub> F/EG electrolyte and annealed at 400 °C for 2 h in air.	152
Table 4.13	Electrolyte properties comparison before anodization	163
Table 4.14	Structural characteristic of FS-ZNTs prepared in H <sub>2</sub> O <sub>2</sub> /NH <sub>4</sub> F/EG electrolyte at different applied voltages for 1 h.	165
Table 4.15	Quantification of phase of FS-ZNTs annealed at different temperatures.	174
Table 4.16	Surface area measurement of as-anodized and annealed FS-ZNTs.	173
Table 4.17	Sample labelling.	181
Table 4.18	Excitation and emission spectra and corresponding photon energy.	184

Table 4.19	Bandgap energy ( $E_g$ ) and band edge positions of the valence band ( $E_{VB}$ ) and conduction band ( $E_{CB}$ ) of ZNTs formed in EG added to it varying oxidants.	186
Table 4.20	Photocatalytic performance comparison under UV light (T and M $ZrO_2$ is for tetragonal and monoclinic $ZrO_2$ respectively).	188
Table 4.21	Photocurrent density at 0.5 $V_{Ag/AgCl}$ and 1 $V_{Ag/AgCl}$ of annealed ZNTs under UV light.	192
Table 4.22	Photocurrent density at 0.5 $V_{Ag/AgCl}$ and 1 $V_{Ag/AgCl}$ of annealed ZNTs under visible light.	194
Table 4.23	Percentage of $\alpha$ - $Fe_2O_3$ and $Fe_3O_4$ in FNPs formed in $H_2O/NH_4F/EG$ electrolyte and annealed at various temperatures.	202
Table 4.24	Raman shift of FNPs formed in $H_2O/NH_4F/EG$ and annealed at 300 – 900 °C.	204
Table 4.25	List of lattice fringes observed from HRTEM.	205
Table 4.26	Percentage of atomic concentration in FNPs formed in $KOH/NH_4F/EG$ electrolyte and annealed at 400 °C.	214
Table 4.27	Comparison of the electrolyte and oxide properties in $KOH/NH_4F/EG$ and $H_2O/NH_4F/EG$ electrolyte.	216
Table 4.28	Comparison of the electrolyte and oxide properties in $LiOH/NH_4F/EG$ and $KOH/NH_4F/EG$ electrolyte.	224
Table 4.29	Comparison of the product of anodization of Fe in $H_2O_2/NH_4F/EG$ and $H_2O/NH_4F/EG$ electrolyte.	226
Table 4.30	Sample labelling and morphologies.	232
Table 4.31	Bandgap energy ( $E_g$ ) and band edge positions of the valence band ( $E_{VB}$ ) and conduction band ( $E_{CB}$ ) of FNPs and FNTs formed in EG added to it varying oxidants.	236
Table 4.32	Photocurrent density at 0.5 $V_{Ag/AgCl}$ and 1 $V_{Ag/AgCl}$ of annealed FNPs and FNTs under visible light.	239

## LIST OF FIGURES

		Page
Figure 1.1	The position of photoanode in a PEC cell.	4
Figure 1.2	ZrO <sub>2</sub> or $\alpha$ -Fe <sub>2</sub> O <sub>3</sub> as photocatalyst to treat water from dyes contamination.	6
Figure 1.3	Practical uses of solar energy for electricity generation and water purification.	7
Figure 1.4	Schematic illustration for nanopores and nanotubes metal oxides formation by anodization as photoactive materials.	10
Figure 1.5	Band gap modification of photoactive oxide semiconductors by oxygen vacancies or impurities (where VB and CB is valence band and conduction band respectively).	11
Figure 1.6	In a thin compact film (a), photogenerated carriers must traverse the entire thickness of the film, $\alpha^{-1}$ (where $\alpha$ is the absorption coefficient), before collection. In a nanopores film (b) and nanotube-array film (c), carriers must only reach the nanotube surface before recombination.	13
Figure 2.1	Microstructure of anodized Zr in aqueous electrolyte : (a) anodic compact oxide film with magnification x10,000 (Cox, 1970), (b) anodic compact oxide film after anodization for 10 min with magnification x11,300 (Archibald and Leach, 1977b), (c) anodic nanoporous oxide (Tsuchiya <i>et al.</i> , 2005b), (d) anodic ZNTs formed in (NH <sub>4</sub> ) <sub>2</sub> SO <sub>4</sub> +NH <sub>4</sub> F electrolyte (Tsuchiya <i>et al.</i> , 2005a; Tsuchiya <i>et al.</i> , 2005c), and (e) anodic ZNTs formed in HF electrolyte (Lee and Smyrl, 2005). Insets in (d) and (e) are cross section image.	26
Figure 2.2	Oxide layer thickness vs. anodization time for tubular arrays grown at 20 V in (NH <sub>4</sub> ) <sub>2</sub> SO <sub>4</sub> +NH <sub>4</sub> F (aqueous electrolyte) and for arrays grown at 20 V in ethylene glycol–glycerol (50:50)+NH <sub>4</sub> F+H <sub>2</sub> O. In the inset images the cross section of the sample anodized for 3 h in electrolyte (a) and 24 h in electrolyte (b) is shown (Berger <i>et al.</i> , 2008a).	28
Figure 2.3	The stages of porous structure development. Adapted from (Parkhutik and Shershulsky, 1992).	33

Figure 2.4	A schematic illustrating the anodization of Zr in fluoride added electrolyte. Adapted from (Amer <i>et al.</i> , 2014).	35
Figure 2.5	A schematic of nanotube formation. Adapted from (Berger <i>et al.</i> , 2011).	37
Figure 2.6	Bright field TEM of FIB (Focused Ion Beam) of Zr anodized at 40 V in NH <sub>4</sub> F/glycerol with: (a) no added H <sub>2</sub> O (Muratore <i>et al.</i> , 2011b), and (b) 5 vol.% added H <sub>2</sub> O (Muratore <i>et al.</i> , 2011a).	37
Figure 2.7	A schematic diagram of the formation of double-layered nanotubes during anodization voltage changing. Adapted from (Fang <i>et al.</i> , 2012a).	38
Figure 2.8	Influence of H <sub>2</sub> O content in glycerol/NH <sub>4</sub> F with 0 – 5 vol.% H <sub>2</sub> O: (a) – (c) according to (Berger <i>et al.</i> , 2008b) and (d) – (f) according to (Muratore <i>et al.</i> , 2011a).	40
Figure 2.9	Linear relationship between applied voltage and: (a) interpore distance (Berger <i>et al.</i> , 2008b), (b) diameter and length of ZNTs (Wang and Luo, 2011).	43
Figure 2.10	Relationship between anodization time and: (a) ZNTs thickness formed at 30 V in glycerin/NH <sub>4</sub> F/H <sub>2</sub> O electrolyte (Wang and Luo, 2011) and (b) ZNTs length, diameter, and wall thicknes formed at 50 V in glycerol/formamide/NH <sub>4</sub> F/H <sub>2</sub> O electrolyte (Amer <i>et al.</i> , 2014).	45
Figure 2.11	XRD patterns of ZNTs annealed at different temperatures in air: (a) annealed ZNTs on Zr metal (Zhao <i>et al.</i> , 2008a), and (b) freestanding ZNTs (Fang <i>et al.</i> , 2011).	54
Figure 2.12	SEM images of ZNTs annealed at different temperatures in air: (a) 400 °C, (b) 500 °C, (c) 600 °C, (d) 700 °C, (e) 800 °C, and (f) 900 °C. (Fang <i>et al.</i> , 2011).	55
Figure 2.13	The energy band positions for ZrO <sub>2</sub> relatives to redox levels of H <sub>2</sub> O dissociation. CB is conduction band; VB is valence band.	56
Figure 2.14	PL spectra of ZNTs: (a) as-anodized and (b) annealed at 400 °C (Fang <i>et al.</i> , 2013).	57

Figure 2.15	(a) FTIR spectra of anodic ZNTs : (i) as-anodized, annealed at (ii) 200 °C, (iii) 400 °C, (iv) 600 °C, and (v) 800 °C (Guo <i>et al.</i> , 2009b), and (b) A wide scan XPS spectra of anodic ZNTs (Shin and Lee, 2009).	61
Figure 2.16	FESEM image of (a) ZNTs and (b) ZNTs after deposition of ZrN; (c) Photocurrent of ZNTs and ZNTs after deposition of ZrN. Bare NTs is for ZNTs and 10 – 142 cycles indicates the number of atomic layer deposition cycles of ZrN (Amer <i>et al.</i> , 2016).	63
Figure 2.17	The typical morphology of anodic $\alpha$ -Fe <sub>2</sub> O <sub>3</sub> nanostructured as photoanodes. Type A and B are SEM images from Lee <i>et al.</i> , 2014. Type C and D are SEM images from Mushove <i>et al.</i> , 2015.	68
Figure 2.18	The energy band positions for $\alpha$ -Fe <sub>2</sub> O <sub>3</sub> relatives to redox levels of H <sub>2</sub> O dissociation. CB is conduction band; VB is valence band.	72
Figure 3.1	Flow chart of the experimental works.	85
Figure 3.2	A photograph and schematic illustration of anodization set-up.	88
Figure 3.3	Flow chart of parameter studied on anodization of Zr.	89
Figure 3.4	Flow chart of parameter studied on anodization of Fe.	91
Figure 3.5	Schematic illustration of equipments and setup in anodization process.	93
Figure 3.6	Experimental set-up for photocurrent measurement.	94
Figure 3.7	Experimental set-up for MO degradation.	96
Figure 4.1	FESEM image of anodic ZrO <sub>2</sub> formed at 60 V for 1 h in EG electrolyte containing 0.27 wt.% NH <sub>4</sub> F: (a) cross sectional view, (b) surface view, (c) high magnification of (a), and (d) high magnification of (b).	105
Figure 4.2	Mechanism of anodic ZrO <sub>2</sub> coral-like morphology formation in NH <sub>4</sub> F/EG electrolyte: (a) bare metal, (b) barrier oxide, (c) pits, (d) pores, and (e) porous anodic ZrO <sub>2</sub> .	107
Figure 4.3	FESEM image of anodic ZrO <sub>2</sub> formed in EG	109

electrolyte containing 0.07 wt.%  $\text{NH}_4\text{F}$  and  $\ll 100 \mu\text{L}$   $\text{H}_2\text{O}$  at (a) 40 V and (c) 60 V; anodic  $\text{ZrO}_2$  formed in EG electrolyte containing 0.27 wt.%  $\text{NH}_4\text{F}$  and  $\ll 100 \mu\text{L}$   $\text{H}_2\text{O}$  at (b) 40 V and (e) 60 V; anodic  $\text{ZrO}_2$  formed in formed in EG electrolyte containing 0.7 wt.%  $\text{NH}_4\text{F}$  and  $\ll 100 \mu\text{L}$   $\text{H}_2\text{O}$  at (c) 40 V and (f) 60 V.

Figure 4.4	FESEM image of ZNTs formed at 60 V for 1 h in EG electrolyte containing 0.27 wt.% $\text{NH}_4\text{F}$ and $\ll 100 \mu\text{L}$ $\text{H}_2\text{O}$ : (a) cross sectional view (b) top view; (c) TEM image of ZNTs at bottom part and (d) single nanotube.	110
Figure 4.5	Current density versus time plot for anodized Zr at 60 V for 1 h in EG electrolyte containing 0.7 wt.%, 0.27 wt.% and 0.7 wt.% $\text{NH}_4\text{F}$ , and $\ll 100 \mu\text{L}$ $\text{H}_2\text{O}$ .	111
Figure 4.6	Mechanism of ZNTs formation in EG electrolyte containing 0.27 wt.% $\text{NH}_4\text{F}$ and $\ll 100 \mu\text{L}$ $\text{H}_2\text{O}$ .	113
Figure 4.7	XRD patterns of ZNTs: as-anodized and annealed at 400 °C. ZNTs formed in $\ll 100 \mu\text{L}$ $\text{H}_2\text{O}/0.27$ wt.% $\text{NH}_4\text{F}/\text{EG}$ at 60 V for 1 h.	115
Figure 4.8	HRTEM images of ZNTs annealed at 400 °C. ZNTs formed in $\ll 100 \mu\text{L}$ $\text{H}_2\text{O}/0.27$ wt.% $\text{NH}_4\text{F}/\text{EG}$ at 60 V for 1 h.	115
Figure 4.9	PL spectra of ZNTs annealed at 400 °C. ZNTs formed in $\ll 100 \mu\text{L}$ $\text{H}_2\text{O}/0.27$ wt.% $\text{NH}_4\text{F}/\text{EG}$ at 60 V for 1 h.	115
Figure 4.10	FESEM images of ZNTs formed in 0.27 wt.% $\text{NH}_4\text{F}/\text{EG}$ with: (a) $\ll 100 \mu\text{L}$ , (b) 0.5 mL, and 3 mL $\text{H}_2\text{O}$ at 60 V for 1 h.	117
Figure 4.11	TEM images of ZNTs formed in 0.27 wt.% $\text{NH}_4\text{F}/\text{EG}$ with: (a) $\ll 100 \mu\text{L}$ , (b) 3 mL $\text{H}_2\text{O}$ at 60 V for 1 h.	117
Figure 4.12	FESEM images of ZNTs formed at 60 V for 1 h in EG electrolyte containing 0.27 wt.% $\text{NH}_4\text{F}$ and 1.0 M KOH : (a) 0.5 mL , (b) 1.0 mL, (c) 2.0 mL, (d) 3.0 mL, and (e) 4.0 mL.	122
Figure 4.13	Schematic illustration of ZNTs formation in KOH/ $\text{NH}_4\text{F}/\text{EG}$ electrolyte: (a) pores formation, (b) nanotubes formation, and (c) double layer nanotubes formation.	123



Figure 4.14	XRD pattern of ZNTs formed at 60 V for 1 h in EG electrolyte containing 0.27 wt.% NH <sub>4</sub> F and 1.0 M KOH : (a) 0.5 mL , (b) 1.0 mL, (c) 2.0 mL, (d) 3.0 mL, and (e) 4.0 mL. ZNTs were annealed at 400 °C for 2 h in air.	124
Figure 4.15	FESEM and TEM images of ZNTs formed at 60 V for 1 h in EG electrolyte containing 0.27 wt.% NH <sub>4</sub> F and 3 mL of : (a) 0.5 M , (b) 1.0 M, (c) 2.0 M, and (d) 3.0 M KOH.	126
Figure 4.16	XRD pattern of ZNTs formed at 60 V for 1 h in EG electrolyte containing 0.27 wt.% NH <sub>4</sub> F and 3 mL of : (a) 0.5 M , (b) 1.0 M, (c) 2.0 M, and (d) 3.0 M KOH. ZNTs were annealed at 400 °C for 2 h in air.	128
Figure 4.17	FTIR spectra of ZNTs formed at 60 V for 1 h in EG electrolyte containing 0.27 wt.% NH <sub>4</sub> F and 3 mL of : (a) 0.5 M , (b) 1.0 M, (c) 2.0 M, and (d) 3.0 M KOH. ZNTs were annealed at 400 °C for 2 h in air.	129
Figure 4.18	(a) Back-scattered FESEM image of anodized Zr sheet in EG electrolyte containing 0.27 wt.% NH <sub>4</sub> F and 1.0 M KOH. Secondary electron FESEM images of anodized Zr sheet in respected electrolyte formed at: (b) 20 V , (c) 40 V, (d) 60 V, (e) 80 V, and (f) 100 V for 1 h.	131
Figure 4.19	TEM images of ZNTs prepared in EG electrolyte containing 0.27 wt.% NH <sub>4</sub> F and 1.0 M KOH at: (a) 20 V , (b) 40 V, (c) 60 V, (d) 80 V, and (e-f) 100 V for 1 h.	131
Figure 4.20	Diameter and length of ZNTs prepared in KOH/NH <sub>4</sub> F/EG electrolyte at 20 – 100 V for 1 h.	132
Figure 4.21	Schematic illustration of double layered ZrO <sub>2</sub> nanotubes formation in KOH/NH <sub>4</sub> F/EG electrolyte at 20 – 100 V.	133
Figure 4.22	XRD pattern for anodized Zr sheet in EG electrolyte containing 0.27 wt.% NH <sub>4</sub> F and 1.0 M KOH at: (a) 20 V , (b) 40 V, (c) 60 V, (d) 80 V, and (e) 100 V for 1 h. ZNTs were annealed at 450 °C for 2 h.	134
Figure 4.23	(A) XRD pattern of ZNTs formed in KOH/NH <sub>4</sub> F/EG: (a) as-anodized, annealed at (b) 300 °C, (c) 400 °C, (d) 450 °C, (e) 500 °C, and (f) 600 °C for 2 h; (B) XPS spectrum of O 1s: 400 °C annealed sample.	136

Figure 4.24	PL spectra of ZNTs anodized in KOH/NH <sub>4</sub> F/EG electrolyte: (a) as-anodized, and (b) annealed at 400 °C.	137
Figure 4.25	(A) XPS and (B) FTIR spectra of ZNTs formed in KOH/NH <sub>4</sub> F/EG electrolyte: (a) as-anodized, and (b) annealed at 400 °C.	138
Figure 4.26	(A) TEM images of ZNTs formed in KOH/NH <sub>4</sub> F/EG electrolyte and annealed at 400 °C, (B) HRTEM, and (C) Elemental mapping of Zr, F, and O from ZNTs.	140
Figure 4.27	(A) FESEM images and (B) TEM images of ZNTs formed at 60 V for 1 h in EG electrolyte containing 0.27 wt.% NH <sub>4</sub> F and 1 mL of : (a) 0.5 M , (b) 1.0 M, (c) 2.0 M, and (d) 3.0 M LiOH.	143
Figure 4.28	Diameter and length of ZNTs prepared in 0.5 – 3.0 M LiOH/NH <sub>4</sub> F/EG electrolyte for 1 h.	144
Figure 4.29	FTIR spectra of ZNTs prepared in NH <sub>4</sub> F/EG electrolyte containing: (a) 0.5 M, (b) 1.0 M, (c) 2.0 M, and (d) 3.0 M LiOH annealed at 400 °C for 2 h in air.	145
Figure 4.30	FESEM images of ZNTs formed in LiOH/NH <sub>4</sub> F/EG electrolyte at: (a) 20 V, (b) 40 V, (c) 60 V, (d) 80 V and (e) 100 V for 1 h.	146
Figure 4.31	TEM images of ZNTs formed in LiOH/NH <sub>4</sub> F/EG electrolyte at: (a) 20 V, (b) 40 V, (c) 60 V, (d) 80 V and (e) 100 V for 1 h.	147
Figure 4.32	Diameter and length of ZNTs prepared in LiOH/NH <sub>4</sub> F/EG electrolyte at 20 – 100 V for 1 h.	147
Figure 4.33	A wide scan XPS spectrum and spectra of F 1s, N 1s, C 1s, and Li 1s of as-anodized ZNTs formed in LiOH/NH <sub>4</sub> F/EG electrolyte: (a) cleaned sample, and (b) non-cleaned sample.	149
Figure 4.34	FTIR spectra of as-anodized ZNTs formed in LiOH/NH <sub>4</sub> F/EG electrolyte: (a) cleaned sample, and (b) non-cleaned sample.	150
Figure 4.35	Schematic illustration of anodic ZrO <sub>2</sub> nanotubes formation in LiOH/NH <sub>4</sub> F/EG electrolyte: (a) pore formation, (b) tube formation.	151

Figure 4.36	XRD pattern for anodized Zr sheet in EG electrolyte containing 0.27 wt.% $\text{NH}_4\text{F}$ and 1.0 M $\text{LiOH}$ at: (a) 20 V, (b) 40 V, (c) 60 V, (d) 80 V, and (e) 100 V and annealed at 400 °C for 2 h.	152
Figure 4.37	(A) XRD pattern of as-anodized ZNTs formed in $\text{LiOH}/\text{NH}_4\text{F}/\text{EG}$ , (B) Raman spectrum of the as-anodized sample, and (C) XRD pattern of ZNTs annealed at: (a) 400 °C, (b) 450 °C, (c) 500 °C, and (d) 600 °C for 2 h.	153
Figure 4.38	PL spectra of ZNTs formed in $\text{LiOH}/\text{NH}_4\text{F}/\text{EG}$ electrolyte: (a) as-anodized, and (b) annealed at 400 °C.	154
Figure 4.39	Survey XPS spectra of ZNTs formed in $\text{LiOH}/\text{NH}_4\text{F}/\text{EG}$ electrolyte: (a) as-anodized, and (b) annealed at 400 °C.	155
Figure 4.40	XPS spectra of O 1s of: (a) the as-anodized ZNTs formed in $\text{LiOH}/\text{NH}_4\text{F}/\text{EG}$ electrolyte and (b) the 400° annealed ZNTs.	157
Figure 4.41	FTIR spectra of ZNTs formed in $\text{LiOH}/\text{NH}_4\text{F}/\text{EG}$ electrolyte: (a) as-anodized sample, (b) 400 °C sample, and (c) 600 °C sample.	158
Figure 4.42	Illustration of: (a) nanocrystalline tetragonal in the as-anodized of ZNTs formed in $\text{LiOH}/\text{NH}_4\text{F}/\text{EG}$ electrolyte, (b) Crystalline oxide in the 400 °C sample and their atomic concentration recorded from XPS.	159
Figure 4.43	Elemental mapping of Li, Zr, O and F obtained from ZNTs formed in $\text{LiOH}/\text{NH}_4\text{F}/\text{EG}$ electrolyte and annealed at 400 °C.	159
Figure 4.44	Back-scattered FESEM images of anodic $\text{ZrO}_2$ films formed in (a) $\text{H}_2\text{O}/\text{NH}_4\text{F}/\text{EG}$ and (b) $\text{H}_2\text{O}_2/\text{NH}_4\text{F}/\text{EG}$ . Secondary electron FESEM image of $\text{ZrO}_2$ films formed in $\text{H}_2\text{O}_2/\text{NH}_4\text{F}/\text{EG}$ : (c) surface layer nanotubes, and (d) internal layer nanotubes.	162
Figure 4.45	FESEM images of anodized Zr in $\text{H}_2\text{O}_2/\text{NH}_4\text{F}/\text{EG}$ electrolyte for 1 h at: (a) 20 V, (b) 40 V, (c) 60 V, (d) 80 V, and (e) 100 V.	164
Figure 4.46	TEM images of FS-ZNTs prepared in $\text{H}_2\text{O}_2/\text{NH}_4\text{F}/\text{EG}$ electrolyte at different applied voltages: (a) 20 V, (b – c) 40 V, (d) 60 V, (e) 80 V	165

and (f) 100 V for 1 h.

Figure 4.47	Current density transient during the formation of ZNTs in $\text{H}_2\text{O}_2/\text{NH}_4\text{F}/\text{EG}$ electrolyte at 20, 40, and 60 V. Insets: TEM images of as-anodized FS-ZNTs formed at 40 V after 10 s, 60 s, 5 min, and 30 min of anodization.	166
Figure 4.48	Formation mechanism of ZNTs formed in $\text{H}_2\text{O}_2/\text{NH}_4\text{F}/\text{EG}$ electrolyte.	168
Figure 4.49	(a) Craters at nanotubes bottom (arrows A) due to high pressure of oxygen gas accumulation (b) Tiny holes at nanotubes bottom (arrows B) and open-ended nanotubes (area C), (c – g) Formation mechanism of FS-ZNTs.	170
Figure 4.50	XRD of FS-ZNTs anodized in $\text{H}_2\text{O}_2/\text{NH}_4\text{F}/\text{EG}$ electrolyte (a) as-anodized and annealed in air at: (b) 200 °C, (c) 300 °C, (d) 400 °C, (e) 450 °C, (f) 500 °C, and (g) 600 °C.	172
Figure 4.51	TEM images of FS-ZNTs anodized in $\text{H}_2\text{O}_2/\text{NH}_4\text{F}/\text{EG}$ electrolyte and annealed in air at: (a) 450 °C and (b) 600 °C.	172
Figure 4.52	HRTEM images of FS-ZNTs anodized in $\text{H}_2\text{O}_2/\text{NH}_4\text{F}/\text{EG}$ electrolyte and annealed at: (a) 450 °C and (b) 600 °C in air with corresponding SAED image.	174
Figure 4.53	PL spectra of FS-ZNTs anodized in $\text{H}_2\text{O}_2/\text{NH}_4\text{F}/\text{EG}$ electrolyte: (a) as-anodized and annealed at 300 °C and (b) annealed at 400, 450 and 600 °C.	177
Figure 4.54	(A) Survey spectra of FS-ZNTs anodized in $\text{H}_2\text{O}_2/\text{NH}_4\text{F}/\text{EG}$ electrolyte and spectra of: (B) F 1s, (C) O 1s, (D) Zr 3d, and (E) C 1s; (a) as-anodized sample and (b) 450 °C sample.	178
Figure 4.55	Possible PL mechanisms of FS-ZNTs.	179
Figure 4.56	FTIR spectra of ZNTs formed in $\text{H}_2\text{O}_2/\text{NH}_4\text{F}/\text{EG}$ electrolyte: (a) as-anodized sample and after annealing at: (b) 450 °C, and (c) 600 °C.	180
Figure 4.57	Diameter and length of ZNTs formed in each electrolyte ( $\text{H}_2\text{O}$ , KOH, LiOH derived ZNTs were anodized at 60 V whereas $\text{H}_2\text{O}_2$ derived ZNTs was anodized at 40V).	182

Figure 4.58	Percentage of tetragonal (T) and monoclinic (M) ZrO <sub>2</sub> in ZNTs formed in EG electrolyte added with different oxidants. ZNTs were annealed at 400 ± 50 °C.	182
Figure 4.59	FTIR spectra of ZNTs formed in each electrolyte. ZNTs were annealed at 400 ± 50 °C.	183
Figure 4.60	PL spectra of ZNTs formed in each electrolyte. ZNTs were annealed at 400 ± 50 °C.	184
Figure 4.61	Bandgap energy of ZNTs formed in each electrolyte. ZNTs were annealed at 400 ± 50 °C.	185
Figure 4.62	Photocatalytic performance (degradation of MO) of annealed ZNTs under UV light.	188
Figure 4.63	A band diagram of FS-ZNTs and photocatalytic mechanism of the oxide.	190
Figure 4.64	Photocatalytic performance (degradation of MO) of annealed ZNTs under visible light. Inset is magnification.	191
Figure 4.65	Photocurrent density-potential of annealed ZNTs under UV light. Inset is magnification.	192
Figure 4.66	Photocurrent density-potential of annealed ZNTs (formed in H <sub>2</sub> O and LiOH added electrolyte) under UV and visible light. Inset is magnification.	193
Figure 4.67	FESEM image of anodic Fe <sub>2</sub> O <sub>3</sub> formed in EG electrolyte containing 3 mL H <sub>2</sub> O and various NH <sub>4</sub> F content: (a) (d) 0.17 wt.%, (b) (e) 0.27 wt.%, and (c) (f) 0.37 wt.% at 50 V for 15 min.	195
Figure 4.68	FESEM images of FNPs prepared by anodizing Fe in H <sub>2</sub> O/NH <sub>4</sub> F/EG: (a) film cross-section, (b) film surface and TEM images showing (c) the pore channels and (d) the ordered pores.	196
Figure 4.69	Mechanism of anodic FNPs formation in H <sub>2</sub> O/NH <sub>4</sub> F/EG electrolyte: (a) bare metal, (b) barrier oxide, (c) pits, (d-e) pores, and (e) ordered porous anodic Fe <sub>2</sub> O <sub>3</sub> .	199
Figure 4.70	FESEM images of iron oxide films formed in H <sub>2</sub> O/NH <sub>4</sub> F/EG and annealed for 2 h at different temperatures: (a) as-anodized, (b) 300 °C, (c) 450 °C, (d) 500 °C, (e) 600 °C, and (f) 900 °C.	200

Figure 4.71	XRD pattern of (a) Fe foil and nanoporous iron oxide films formed in H <sub>2</sub> O/NH <sub>4</sub> F/EG : (b) as-anodized, and annealed at: (c) 300 °C, (d) 450 °C, (e) 500 °C, (f) 600 °C and (g) 900 °C under in nitrogen.	202
Figure 4.72	Raman spectra of (a) Fe foil, and nanoporous anodic iron oxide films formed in H <sub>2</sub> O/NH <sub>4</sub> F/EG and annealed at: (b) 300 °C, (c) 450 °C, (d) 500 °C, (e) 600 °C and (f) 900 °C.	203
Figure 4.73	(a) HRTEM image of FNPs formed in H <sub>2</sub> O/NH <sub>4</sub> F/EG electrolyte and annealed at 450 °C and (b) corresponding SAED pattern.	204
Figure 4.74	FTIR spectra of FNPs formed in H <sub>2</sub> O/NH <sub>4</sub> F/EG electrolyte: (a) as-anodized sample and (b) after annealing at 450 °C.	206
Figure 4.75	FESEM image of anodic FNPs formed in EG electrolyte containing 1 mL KOH and various NH <sub>4</sub> F content: (a) (d) 0.17 wt.%, (b) (e) 0.27 wt.%, and (c) (f) 0.37 wt.% at 50 V for 10 min.	207
Figure 4.76	Current density versus time plot for anodized Fe at 50 V for 10 min in EG electrolyte containing 0.17 wt.%, 0.27 wt.% and 0.37 wt.% NH <sub>4</sub> F, and 1 mL KOH.	209
Figure 4.77	Mechanism of FNPs formation in high flouride content electrolyte (EG electrolyte containing 0.37 wt.% NH <sub>4</sub> F, and 1 mL KOH) at 50 V for 10 min.	209
Figure 4.78	XRD patterns of FNPs formed in KOH/NH <sub>4</sub> F/EG : (b) as-anodized, and annealed at 400 °C.	211
Figure 4.79	Raman spectra of FNPs formed in KOH/NH <sub>4</sub> F/EG: (b) as-anodized, and annealed at 400 °C.	211
Figure 4.80	(a) TEM and (b) HRTEM images of as-anodized FNPs formed in KOH/NH <sub>4</sub> F/EG, and (c) HRTEM of annealed FNPs at 400 °C.	212
Figure 4.81	(a) XPS survey spectra of FNPs anodized in KOH/NH <sub>4</sub> F/EG electrolyte and annealed at 400 °C; XPS spectra of: (b) C 1s, (c) O 1s, and (d) Fe 2p.	214
Figure 4.82	FTIR spectra of (a) FNPs formed in KOH/NH <sub>4</sub> F/EG electrolyte: (i) as-anodized sample and (ii) after annealing at 400 °C; (b) the as-anodized FNPs	215

	formed in: (i) H <sub>2</sub> O/NH <sub>4</sub> F/EG and (ii) KOH/NH <sub>4</sub> F/EG electrolyte.	
Figure 4.83	FESEM image of FNPs formed in LiOH/NH <sub>4</sub> F/EG electrolyte at 50 V for 10 min: (a) top view and (b) cross sectional view.	217
Figure 4.84	Raman spectra of FNPs formed in LiOH/NH <sub>4</sub> F/EG: (b) as-anodized, and annealed at 400 °C in nitrogen.	218
Figure 4.85	FTIR spectra of (a) FNPs formed in LiOH/NH <sub>4</sub> F/EG electrolyte: (i) as-anodized sample and (ii) after annealing at 400 °C; (b) the as-anodized FNPs formed in: (i) LiOH/NH <sub>4</sub> F/EG and (ii) KOH/NH <sub>4</sub> F/EG electrolyte.	219
Figure 4.86	(a) TEM image of FNPs formed in LiOH/NH <sub>4</sub> F/EG, and (b) HRTEM image of annealed FNPs at 400 °C in nitrogen.	220
Figure 4.87	(a) XPS survey spectra of FNPs anodized in LiOH/NH <sub>4</sub> F/EG electrolyte and spectra of: (b) O 1s, (c) F 1s, (d) Li 1s, (e) N 1s and (f) Fe 2p; (black line) as-anodized sample and (blue line) 400 °C annealed sample.	222
Figure 4.88	PL spectrum of FNPs anodized in LiOH/NH <sub>4</sub> F/EG electrolyte and annealed at 400 °C.	223
Figure 4.89	FESEM image of FNTs formed in H <sub>2</sub> O <sub>2</sub> /NH <sub>4</sub> F/EG electrolyte at 50 V for 15 min: (a) cross sectional view and (b) top view.	225
Figure 4.90	Schematic illustration of anodization of Fe in: (a) H <sub>2</sub> O/NH <sub>4</sub> F/EG and (b) H <sub>2</sub> O <sub>2</sub> /NH <sub>4</sub> F/EG electrolyte.	227
Figure 4.91	Raman spectra of FNTs formed in H <sub>2</sub> O <sub>2</sub> /NH <sub>4</sub> F/EG: (b) as-anodized, and annealed at 400 °C.	229
Figure 4.92	FTIR spectra of (a) FNTs formed in H <sub>2</sub> O <sub>2</sub> /NH <sub>4</sub> F/EG electrolyte: (i) as-anodized sample and (ii) after annealing at 400 °C; (b) the as-anodized film formed in: (i) H <sub>2</sub> O <sub>2</sub> /NH <sub>4</sub> F/EG (FNTs) and (ii) H <sub>2</sub> O/NH <sub>4</sub> F/EG electrolyte (FNPs).	230
Figure 4.93	(a) TEM image of FNTs formed in H <sub>2</sub> O <sub>2</sub> /NH <sub>4</sub> F/EG, and (b) HRTEM image of annealed FNTs.	231
Figure 4.94	XPS survey spectrum of FNTs formed in H <sub>2</sub> O <sub>2</sub> /NH <sub>4</sub> F/EG and annealed at 400 °C.	232

Figure 4.95	Diameter and length of FNPs or FNTs formed in each electrolyte (All samples were anodized at 50 V).	233
Figure 4.96	Percentage of $\alpha$ -Fe <sub>2</sub> O <sub>3</sub> (H) and Fe <sub>3</sub> O <sub>4</sub> (M) in FNPs/FNTs formed in EG electrolyte added with different oxidants after annealing at 400 ± 50 °C.	234
Figure 4.97	FTIR spectra of FNPs and FNTs formed in each electrolyte and annealed at 400±50 °C.	235
Figure 4.98	Bandgap energy of annealed FNPs and FNTs formed in each electrolyte.	236
Figure 4.99	Photocurrent density-potential of annealed FNPs and FNTs under visible light. Inset is magnification.	238
Figure 4.100	FESEM image of cross section of FNPs formed in H <sub>2</sub> O/NH <sub>4</sub> F/EG and annealed at 450 °C in: (a) nitrogen and (b) air.	240
Figure 4.101	Photocatalytic performance (degradation of MO) of annealed FNPs/FNTs under visible light.	242
Figure 4.102	A band diagram of FNPs and photocatalytic mechanism of the oxide.	242



## LIST OF ABBREVIATIONS

1-D	1 dimensional
AAO	Anodic aluminium oxide
Al	Aluminum
AM 1.5	Air Mass Solar Spectrum ( $100 \text{ mW cm}^{-2}$ )
BE	Binding energy
BET	Brunauere Emmette Teller
CB	Conduction band
D	Crystallite size
EG	Ethylene glycol
EHPs	Electron-hole pairs
EFTEM	Energy Filtered Transmission Electron Microscopy
ESI	Electron Spectroscopic Imaging
FESEM	Field Emission Scanning Electron Microscopy
FRL	Flouride-rich layer
FTIR	Fourier Transform Infrared
FNPs	$\alpha\text{-Fe}_2\text{O}_3$ nanopores
FNTs	$\alpha\text{-Fe}_2\text{O}_3$ nanotubes
FS-ZNTs	Freestanding $\text{ZrO}_2$ nanotubes
HRTEM	High-Resolution Transmission Electron Microscopy
M	Metal
MO	Methyl orange
NIR	Near infrared
PDF	Powder Diffraction File
PEC	Photoelectrochemical
PL	Photoluminescence
SAED	Selected Area Electron Diffraction
SHE	Standard hydrogen electrode
TEM	Transmission Electron Microscopy
TNTs	$\text{TiO}_2$ nanotubes
UV	Ultraviolet
UV-Vis	Ultraviolet-visible

VB	Valence band
XRD	X-ray Diffraction
XPS	X-ray photoelectron spectroscopy
YSZ	Yttria-stabilized zirconia
ZNTs	ZrO <sub>2</sub> nanotubes

## LIST OF SYMBOLS

%	Percentage
<	Less than
>	Greater than
°	Degree
wt. %	Weight percentage
M	Molarity
ppm	Parts per million
eV	Electron volt
$\lambda$	Wavelength
$h\nu$	Photon energy
$\alpha$	Absorption coefficient
$2\theta$	Diffraction angle
$X$	Electronegativity
$E^e$	Energy of free electrons on the hydrogen scale
$E_g$	Bandgap energy
$E_{VB}$	Valence band edge potential
$E_{CB}$	Conduction band edge potential

**PENGEMBANGAN TIUB NANO ZIRKONIA DAN LIANG NANO FERUM  
OKSIDA MELALUI KAEDAH PENGANODAN UNTUK BAHAN  
TERAKTIF FOTO**

**ABSTRAK**

Tenaga solar boleh digunakan untuk penjanaan elektrik dan pembersihan air. Untuk menangkap foton solar, bahan teraktif foto diperlukan. Walau bagaimanapun, beberapa masalah telah dikenalpasti pada penggunaan oksida sebagai bahan teraktif foto: (1) penggabungan semula pasangan fotojana elektron-lohong, (2) penggunaan sinaran boleh nampak dan (3) oksida amorf membatasi penggunaan. Dalam tesis ini, tiub nano  $\text{ZrO}_2$  (ZNTs), liang nano  $\alpha\text{-Fe}_2\text{O}_3$  (FNPs) dan tiub nano  $\alpha\text{-Fe}_2\text{O}_3$  (FNTs) telah berjaya difabrikasikan dalam elektrolit ammonium fluorit ( $\text{NH}_4\text{F}$ )/glikol etilena (EG) yang mengandungi pelbagai penyedia  $\text{O}^{2-}$  dan/atau  $\text{OH}^-$  ( $\text{H}_2\text{O}$ ,  $\text{KOH}$ ,  $\text{LiOH}$  or  $\text{H}_2\text{O}_2$ ) melalui kaedah penganodan. ZNTs, FNPs dan FNTs digunakan sebagai fotoanod dalam sel fotoelektrokimia (PEC) untuk menghasilkan arusfoto dan sebagai fotopemangkin untuk degradasi metil oren. ZNTs berlapis ganda dimana tiub diameter 45 nm di lapisan atas dan tiub yang lebih besar (140 nm) di lapisan bawah dihasilkan dalam  $\text{KOH}/\text{NH}_4\text{F}/\text{EG}$ . ZNTs dengan panjang 7.4  $\mu\text{m}$  dihasilkan dalam  $\text{LiOH}/\text{NH}_4\text{F}/\text{EG}$ , namun mempunyai permukaan ZNTs ditutupi oleh pencemaran anion/kation ( $\text{OH}^-$ ,  $\text{F}^-$ ,  $\text{CO}_3^{2-}$ ,  $\text{NH}_4^+$ , and  $\text{Li}^+$ ). Sementara itu, ZNTs yang berdiri bebas (FS-ZNTs) difabrikasikan dalam  $\text{H}_2\text{O}_2/\text{NH}_4\text{F}/\text{EG}$  disebabkan oleh kekosongan oksigen yang membantu melemahkan kelekatan ZNTs pada Zr. ZNTs yang dihasilkan dalam  $\text{LiOH}/\text{NH}_4\text{F}/\text{EG}$  mempunyai sebahagian besar kristalit tetragonal  $\text{ZrO}_2$  disebabkan oleh kewujudan kekosongan oksigen,  $\text{OH}^-$  dan bendasing. Setelah penyepuhlindapan, ZNTs mempunyai sebahagian besar monoklinik  $\text{ZrO}_2$  sementara

FS-ZNTs mempunyai sebahagian besar tetragonal  $\text{ZrO}_2$  dengan jurang tenaga  $\sim 5$  eV. FS-ZNTs menunjukkan 34% degradasi MO setelah 2 jam terdedah di bawah cahaya UV, sementara 9.5% degradasi MO diperhatikan setelah 2 jam terdedah cahaya tampak. Ini menunjukkan ZNTs dapat diaktifkan di bawah cahaya tampak untuk degradasi MO. ZNTs yang terbuat dalam LiOH menghasilkan arusfoto  $2.18 \text{ mA cm}^{-2}$  pada  $1 \text{ V}_{\text{Ag}/\text{AgCl}}$  dibawah UV, tetapi di bawah cahaya tampak arusfoto terhasil sangat rendah  $1.69 \times 10^{-4} \text{ mA cm}^{-2}$  pada  $1 \text{ V}_{\text{Ag}/\text{AgCl}}$ . ZNTs mungkin tidak sesuai digunakan sebagai fotoanod dalam sel PEC dibawah cahaya tampak, walaupun jurang tenaga telah disempitkan disebabkan kecacatan dalam jurang tenaga. Bahan dengan jurang tenaga yang lebih kecil  $\alpha\text{-Fe}_2\text{O}_3$  difabrikasi melalui penganodan besi (Fe) dalam usaha menghasilkan bahan teraktif cahaya tampak. Penganodan Fe dalam  $\text{H}_2\text{O}$ , KOH atau LiOH/ $\text{NH}_4\text{F}$ /EG menghasilkan FNPs. FNPs setelah dianod dalam KOH atau LiOH elektrolit mempunyai FeOOH kristal kerana kandungan  $\text{OH}^-$  yang tinggi. FNTs dengan permukaan berumput terhasil dalam  $\text{H}_2\text{O}_2$ / $\text{NH}_4\text{F}$ /EG. Selepas penyepuhlindapan, FNPs/FNTs mempunyai sebahagian besar fasa  $\alpha\text{-Fe}_2\text{O}_3$ . FNPs yang terbentuk dalam  $\text{H}_2\text{O}$ / $\text{NH}_4\text{F}$ /EG menghasilkan arusfoto tertinggi iaitu  $25.6 \text{ mA cm}^{-2}$  pada  $1 \text{ V}_{\text{Ag}/\text{AgCl}}$  kerana kehadiran  $\alpha\text{-Fe}_2\text{O}_3$  dan lapisan antara muka yang nipis. Arusfoto terendah  $2.8 \text{ mA cm}^{-2}$  pada  $1 \text{ V}_{\text{Ag}/\text{AgCl}}$  dihasilkan daripada FNTs. Arusfoto berkurangan disebabkan oleh morfologi dan kewujudan  $\text{Fe}_3\text{O}_4$ . Penyepuhlindapan mesti dilakukan dalam nitrogen untuk mengurangkan pertumbuhan  $\text{Fe}_3\text{O}_4$ . FNPs yang terbentuk dalam LiOH menunjukkan 34% degradasi MO selepas 2 jam pendedahan cahaya tampak. Sampel ini mempunyai jurang tenaga 2.2 eV dan kecacatan pada 1.9 eV disebabkan oleh kekosongan oksigen mengakibatkan peningkatan kepadatan lohong bebas, lalu meninggikan degradasi MO.

# **DEVELOPMENT OF ZIRCONIA NANOTUBES AND IRON OXIDE NANOPORES BY ANODIZATION METHOD FOR PHOTOACTIVE MATERIAL**

## **ABSTRACT**

Solar energy can be utilized for electricity generation and water purification. To capture solar photons, photoactive materials are required. However, several problems were identified on the use of oxide as photoactive material: (1) recombination of photogenerated electron-hole pairs, (2) visible light utilization and (3) amorphous oxide limits the application. In this thesis, ZrO<sub>2</sub> nanotubes (ZNTs),  $\alpha$ -Fe<sub>2</sub>O<sub>3</sub> nanopores (FNPs) and  $\alpha$ -Fe<sub>2</sub>O<sub>3</sub> nanotubes (FNTs) were successfully fabricated by anodization in ammonium fluoride (NH<sub>4</sub>F)/ethylene glycol (EG) electrolyte containing various O<sup>2-</sup> and/or OH<sup>-</sup> providers (H<sub>2</sub>O, KOH, LiOH or H<sub>2</sub>O<sub>2</sub>) to overcome the mentioned problems. The ZNTs, FNPs and FNTs were used as photoanode in a photoelectrochemical cell to generate photocurrent and as photocatalyst to degrade methyl orange (MO). Double layered ZNTs with top layer tube diameter of 45 nm and larger nanotubes (140 nm) at bottom layer were obtained in KOH/NH<sub>4</sub>F/EG. 7.4  $\mu$ m length ZNTs was formed in LiOH/NH<sub>4</sub>F/EG, however the surface was covered by anion/cation contamination (OH<sup>-</sup>, F<sup>-</sup>, CO<sub>3</sub><sup>2-</sup>, NH<sub>4</sub><sup>+</sup>, and Li<sup>+</sup>). Meanwhile freestanding ZNTs (FS-ZNTs) were fabricated in H<sub>2</sub>O<sub>2</sub>/NH<sub>4</sub>F/EG due to oxygen evolution which aids in weakening the adherence of the ZNTs from Zr. As-anodized ZNTs formed in LiOH/NH<sub>4</sub>F/EG have tetragonal ZrO<sub>2</sub> crystallite due to the existence of oxygen vacancies, OH<sup>-</sup> and impurities. After annealing, ZNTs have majority monoclinic ZrO<sub>2</sub> whereas FS-ZNTs have majority tetragonal ZrO<sub>2</sub> with bandgap of ~5 eV. FS-ZNTs exhibited 34% MO degradation after 2 h of UV light whereas 9.5% MO degradation was observed after 2 h of visible light exposure.

These indicate ZNTs can be activated under visible light to degrade MO. LiOH derived ZNTs with good adherence with Zr generated high photocurrent of 2.18 mA cm<sup>-2</sup> at 1 V<sub>Ag/AgCl</sub> under UV, but under visible light very small current of 1.69 x 10<sup>-4</sup> mA cm<sup>-2</sup> at 1 V<sub>Ag/AgCl</sub> were generated. ZNTs may not suitable to be used as photoanode in a PEC cell under visible light despite the band narrowing due to defects within their energy gap. A smaller bandgap material  $\alpha$ -Fe<sub>2</sub>O<sub>3</sub> was fabricated by anodization of iron (Fe) in an attempt to produce visible light activated material. Anodization of Fe in H<sub>2</sub>O, KOH, or LiOH/NH<sub>4</sub>F/EG produced FNPs. The as-anodized FNPs formed in KOH or LiOH electrolyte have crystalline FeOOH due to the high content of OH<sup>-</sup>. FNTs with grassy surface were formed in H<sub>2</sub>O<sub>2</sub>/NH<sub>4</sub>F/EG. After annealing, FNPs/FNTs have majority  $\alpha$ -Fe<sub>2</sub>O<sub>3</sub> phase. FNPs formed in H<sub>2</sub>O/NH<sub>4</sub>F/EG generated highest photocurrent of 25.6 mA cm<sup>-2</sup> at 1 V<sub>Ag/AgCl</sub> due to the presence of  $\alpha$ -Fe<sub>2</sub>O<sub>3</sub> and thin interfacial layer. The lowest photocurrent of 2.8 mA cm<sup>-2</sup> at 1 V<sub>Ag/AgCl</sub> was produced from FNTs. The reduced photocurrent may be due the morphologies and the existence of Fe<sub>3</sub>O<sub>4</sub>. Annealing must be done in nitrogen to reduce the growth of Fe<sub>3</sub>O<sub>4</sub>. As for the MO degradation, LiOH derived FNPs exhibited 34% degradation after 2 h of visible light exposure. The sample has bandgap energy of 2.2 eV and defect state at 1.9 eV due to oxygen vacancies resulted in increasing free holes density, hence enhanced MO degradation.

# CHAPTER ONE

## INTRODUCTION

### 1.1. Background

This thesis is on the synthesis, characterization and utilization of photoactive semiconductor oxides for energy and environmental protection purposes. Two main materials synthesized in nanoscale were studied:  $ZrO_2$  and  $\alpha\text{-Fe}_2O_3$ . This chapter introduces the background that leads to the use of these photoactive semiconductor oxides as light-to-electric current (photocurrent) converter, and as photocatalyst for water purification from dyes contamination. Problem statements and gap of knowledge on nanostructured  $ZrO_2$  and  $\alpha\text{-Fe}_2O_3$  formation process, and their photoactivity properties are introduced along with the main aim and specific objectives of the thesis.

#### 1.1.1. Electricity generation

One of the driving forces in achieving economic development is energy. Fulfilling energy demand from large number of population is a great challenge especially for developing countries, like Malaysia. As the third largest energy consumer in Southeast Asian countries after Indonesia and Thailand (IEA, 2015), Malaysia's energy demand of 2013 population of nearly 30 million people was 89 million tonnes of oil equivalent. Population and energy demand are predicted to increase to 40 million and 160 million tonnes of oil equivalent respectively in 2040 (Table 1.1), hence the country needs more energy in the future.



**Table 1.1:** Key indicators for Malaysia (IEA, 2015)

Indicator	Unit	Year		
		2000	2013	2040
Population	million	23	30	40
Energy demand	million tonnes of oil equivalent	50	89	160
Electricity demand	TWh	61	124	400
CO <sub>2</sub> emission	million tonnes	118	211	430

According to Malaysia Energy Statistics Handbook 2015 (Tenaga, 2015) natural gas and coal provided about 88% of electricity generation in 2013. Based on IEA forecasting, the country's electricity generation will reach 400 TWh in 2040 with natural gas and coal as the largest sources for electricity generation. Given the continuing dominance of fossil fuels in the country's energy mix, the CO<sub>2</sub> emission will be increased from 211 million tonnes in 2013 to almost 430 million tonnes by 2040 as shown in Table 1.1. The impact on environment caused by CO<sub>2</sub> emission is a serious concern. Therefore, to reduce the dependence on fossil fuels and to limit CO<sub>2</sub> emission, the use of renewable energy source need to be considered.

Among various renewable energies, solar energy is seen as the only source of renewable energy that has high potential to meet energy demands (Lewis and Crabtree, 2005; Lewis and Nocera, 2006), especially in Malaysia. More importantly solar energy does not contribute to CO<sub>2</sub> emission (Solangi *et al.*, 2011). As Malaysia lies entirely in the equatorial region and has abundant solar radiation, the utilization of solar energy is extremely logical for electricity generation. A summary of yearly average solar radiation in various towns in the country is shown in Table 1.2. The Northern region (Mekhilef *et al.*, 2012) has the highest potential hence every effort in converting solar energy for electricity generation is important.

**Table 1.2:** Solar intensity in Malaysia (Mekhilef *et al.*, 2012)

Location	Yearly intensity average (kWh m <sup>-2</sup> )
Kuching	1470
Kuala Lumpur	1571
Johor Bahru	1625
Ipoh	1739
George Town	1785
Bayan Lepas	1809
Kota Kinabalu	1900

Various technologies can be utilized to capture solar energy and turn it into electricity. One way is to capture solar photons by a photoelectrochemical (PEC) cell utilizing aqueous electrolyte and converting them to photocurrent which at the same time can lead to hydrogen generation. PEC-type cells can also have various different functions (Gratzel, 2001), but in this work, focus was given to convert solar to photocurrent. Based on International Union of Pure and Applied Chemistry (IUPAC) Recommendations 2011, definition of photocurrent is photogeneration and movement of charge between two electrodes in a photovoltaic cell or a PEC cell as a result of photoprocesses induced by light absorption (Braslavsky *et al.*, 2011). A PEC cell requires a photoactive material; a material that can be activated under light irradiation, to generate the photocurrent. A photoanode in a PEC cell is consisted of photoactive oxide semiconductor as shown in Figure 1.1. In this thesis, two oxides; ZrO<sub>2</sub> and  $\alpha$ -Fe<sub>2</sub>O<sub>3</sub> made in nanoscale and their ability to generate photocurrent were studied. As shall be explained later, the selected oxide materials also have the properties to split water and through the process of water splitting, hydrogen gas is produced.

One of the advantages of a PEC cell is that hydrogen and oxygen gases are produced at separate electrode. The photogenerated electrons reduce water to form

hydrogen at platinum counter electrode, while holes oxidize water to form oxygen on photoanode. This allows easy separation of these gases without considering post separation. Another advantage of PEC cell is that it can be conducted at room temperature. Hydrogen gas can be converted into electricity and used as chemical fuels to power vehicles.

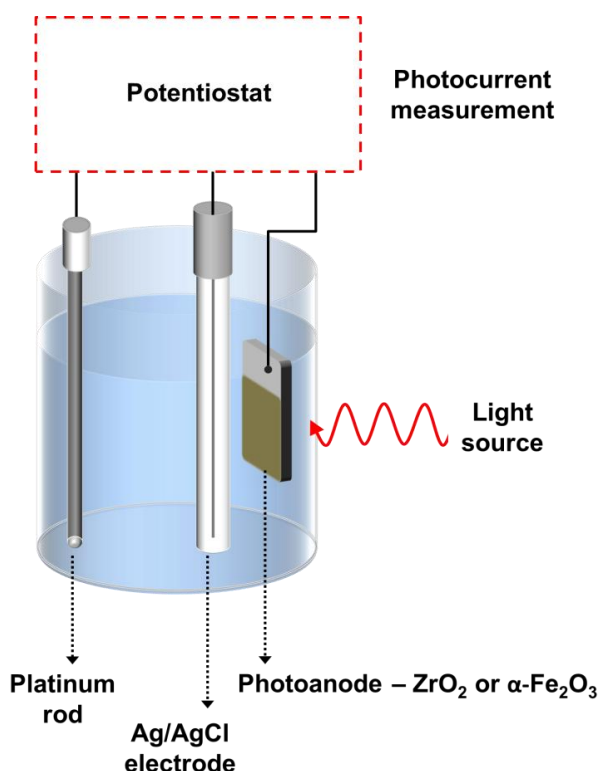


**Figure 1.1:** The position of photoanode in a PEC cell.

### 1.1.2. Dye pollution in water

On a different note, Malaysia is known as a net exporter of textiles and apparel. In 2014 the textiles industry contributed 1.6% share of the country's export of manufactured goods (MIDA, 2015). Investment in the Malaysian textile and clothing industry is expected to increase more than US\$ 3 billion in 2020. Textile industry is also expected to continue fulfilling an important role in the country's economic development. Unfortunately textile industry utilizes huge amount of water

and produces high quantity of waste water. A major source of water pollution from textile industry is the release of dyes into environment during textile fiber dyeing (Pang and Abdullah, 2013). A wide variety of health problems can be caused by dyes contamination, like skin rashes, headaches, diarrhea, muscle and joint pain, dizziness, difficulty in breathing, and irregular heartbeat (Chavan, 2011).

Since the presence of dyes in waste water is unwanted, there are several treatment methods to treat waste water from textile industry before it can be safely release to the environment like adsorption, ion exchange, membrane filtration, biological method (aerobic and anaerobic process), chemical coagulation, and photocatalysis (Pang and Abdullah, 2013). Energy consumption, efficiency, cost and easy operation need to be considered to select the best method. Among various methods mentioned, photocatalysis is believed to be an efficient, relatively easy and a cost effective method to remove dyes in water, thus is seen as a promising technique for water purification (Ajmal *et al.*, 2014; Khataee and Kasiri, 2010).

Referring to IUPAC Recommendations 2011, the definition of photocatalysis is the change in the rate of a chemical reaction or its initiation under the action of ultraviolet, visible, or infrared radiation in the presence of a substance – the photocatalyst – that absorbs light and is involved in chemical transformation of the reaction partners (Braslavsky *et al.*, 2011). It is clearly stated that ultraviolet, visible, or infrared radiation are needed on photocatalysis and all these radiations are included in the solar spectrum. As mentioned, Malaysia has abundant solar radiation, hence the utilization of solar energy for water purification from dye contaminant for instance by photocatalysis will be a potential solution for treating waste water from textile industry in Malaysia. Similar to the materials used to generate useful photocurrent, photoactive oxide semiconductors can be utilized as

photocatalysts (Figure 1.2). Similarly,  $\text{ZrO}_2$  and  $\alpha\text{-Fe}_2\text{O}_3$  were selected to be investigated as photocatalysts in this thesis.

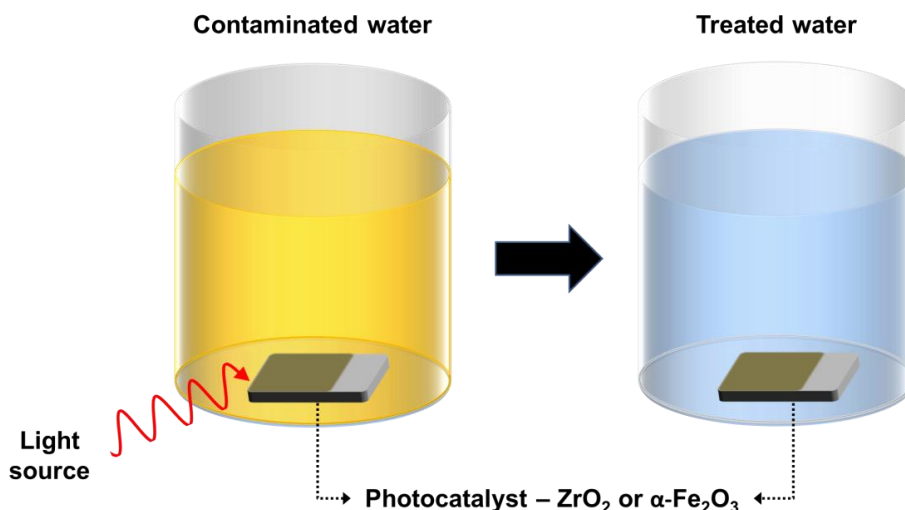


**Figure 1.2:**  $\text{ZrO}_2$  or  $\alpha\text{-Fe}_2\text{O}_3$  as photocatalyst to treat water from dyes contamination.

## 1.2. Photoactive material

Practical uses of solar energy on electricity generation and water purification are summarized in Figure 1.3. To generate photocurrent in a PEC cell and for photocatalysis applications, a material that can be activated under light irradiation is needed (or called photoactive). A semiconductor is a material that can generate electron-hole pairs (EHPs) through optical excitation. The valence band is the highest energy band filled with electrons while conduction band is the lowest unoccupied band. The absorption of photons with larger energy than the band gap of a semiconductor will produce EHPs which are useful carriers to either provide sufficient electric current (photocurrent) or to perform oxidation or reduction process via electron or hole transfers (photocatalyst). To ensure EHPs play the role in driving the photoactivity process, they must not be allowed to recombine and ought to be separated as fast as possible. They must have a long life time until they can

travel to the surface of the semiconductor to be transferred to either adsorbed species or to the electrolyte. Therefore, to able the use of photoactive oxides as photoanode or photocatalyst, the following properties are required:

- high light absorption coefficient (in order  $10^3 \text{ cm}^{-1}$ )
- suitable bandgap energy to produce EHPs
- position of conduction and valence band straddles the redox potential of water
- efficient EHPs separation
- able to transport carrier to semiconductor interface as quick as possible

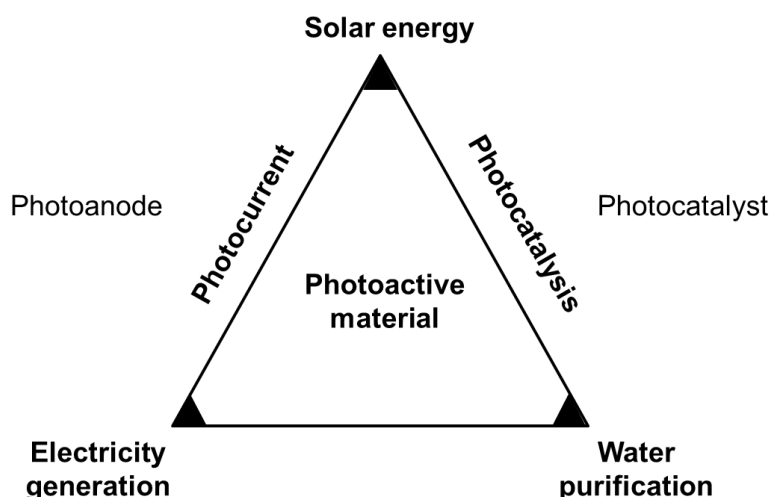


**Figure 1.3:** Practical uses of solar energy for electricity generation and water purification.

As mentioned, there were two semiconductor oxide materials studied here:  $\text{ZrO}_2$  and  $\alpha\text{-Fe}_2\text{O}_3$ .  $\text{ZrO}_2$  is also a wide band gap semiconductor but the high conduction band position is enough to initiate photocatalytic processes in aqueous solution (Asmatulu *et al.*, 2015; Gerischer, 1981).  $\text{ZrO}_2$  exists as monoclinic, tetragonal, and cubic phases (Keramidas and White, 1974). The three phases of  $\text{ZrO}_2$

(monoclinic, tetragonal, and cubic) have bandgap energies of 5.1 eV, 5.2 eV, and 5.2 eV respectively from theoretical data (French *et al.*, 1994) and 3 – 6 eV from experimental data (Anandan *et al.*, 2017; Goharshadi and Hadadian, 2012; McComb, 1996; Nicoloso *et al.*, 1992; Sathyaseelan *et al.*, 2017; Xu *et al.*, 2016). While the monoclinic phase is stable at room temperature, tetragonal or cubic are high temperature phases. Therefore, they must be stabilized at room temperature or else the tetragonal or cubic phase will revert to monoclinic when cooled to room temperature. To stabilize tetragonal and cubic phase at room temperature, ZrO<sub>2</sub> has to be made oxygen deficient (Fabris *et al.*, 2002; Liu *et al.*, 2014). Often this is achieved by Y<sup>3+</sup> or Ce<sup>3+</sup> doping and significant defects are introduced in the oxide. The main defect is oxygen vacancy.

Since ZrO<sub>2</sub> has a rather wide energy gap, it can only be activated under UV irradiation, similar to TiO<sub>2</sub>. Despite its wide bandgap, ZrO<sub>2</sub> has shown significant photoactivity (Emeline *et al.*, 2005). Among various reasons to account for this is the existence of defects which successfully modify the electronic properties of the oxide. In this thesis, ZrO<sub>2</sub> was synthesized as thin film with nanotubular structure by anodization process. The reason of nanostructuring will be explained later but suffice to say is to increase the surface area of the oxide. Anodization process requires oxygen ions migration across oxide film for film growth. The migration is electric field dependent. Because of this, the formed anodic ZrO<sub>2</sub> is often very defective and is consisted of oxygen vacancies (Bashirom *et al.*, 2017; Fang *et al.*, 2013). Two effects are seen from the existence of oxygen defects:

- (i) Stabilization of tetragonal or cubic ZrO<sub>2</sub> at room temperature
- (ii) Modification of electronic band structure of ZrO<sub>2</sub>

while the former is interesting as no dopants are needed for anodic  $\text{ZrO}_2$  to be in tetragonal phase, the latter is useful since the presence of defects levels within the wide bandgap of  $\text{ZrO}_2$  can aid in visible light activation of the oxide. From photoluminescence spectra of tetragonal phase, it was reported that oxygen vacancy narrows the gap to 2.04 eV (Liang *et al.*, 2002). This can be translated to 608 nm wavelength of light (i.e. within visible light region). Oxygen vacancies introduce a level near valence band of  $\text{ZrO}_2$  (Kumar and Ojha, 2015), narrowing the energy gap of the oxide.

$\alpha\text{-Fe}_2\text{O}_3$  on the other hand is already a narrow gap semiconductor with bandgap energy of  $\sim 2.2$  eV, hence light absorption from green-yellow colour in visible region until UV region for EHPs formation is possible. The oxide therefore can be activated readily under solar spectrum.  $\alpha\text{-Fe}_2\text{O}_3$  is abundant and relatively inert in most electrolyte over a wide range of pH (Forster *et al.*, 2015). Iron oxide mostly exists in the form of magnetite ( $\text{Fe}_3\text{O}_4$ ), maghemite ( $\gamma\text{-Fe}_2\text{O}_3$ ) and hematite ( $\alpha\text{-Fe}_2\text{O}_3$ ) (Cornell and Schwertmann, 2003). But among all these phases,  $\alpha\text{-Fe}_2\text{O}_3$  has been used as a photoanode in PEC cells (Bassi *et al.*, 2014; Sivula *et al.*, 2011) to give photocurrent.

Here  $\text{ZrO}_2$  and  $\alpha\text{-Fe}_2\text{O}_3$  films were produced on Zr and Fe foils respectively, with the film consisted of nanotubes or nanopores structure. The International Organization for Standardization (ISO) defines nanomaterial as a material with any external dimensions in the nanoscale or having internal structure or surface structure in the nanoscale (ISO, 2010; Boverhof *et al.*, 2015). The ISO definition of nanoscale is in the range of 1 – 100 nm. The use of photoactive materials in nanoscale has been suggested due to high surface area hence larger area for light absorption is expected (Satsangi *et al.*, 2010). In addition, the use of semiconductor in nanoscale is also to



minimize the distance for photogenerated carriers to reach semiconductor|electrolyte interface, thus reducing the probability of recombination (Walter *et al.*, 2010).

### 1.3. Synthesis method of nanostructured $\text{ZrO}_2$ and $\alpha\text{-Fe}_2\text{O}_3$

There are various different ways to form metal oxide with nanotubular and nanoporous structure such as template based method (Bao *et al.*, 2002; Cochran *et al.*, 2007; Ogihara *et al.*, 2006; Rao *et al.*, 1997), sol-gel (Gundiah *et al.*, 2003; Huo *et al.*, 2014), atomic layer deposition (Bachmann *et al.*, 2007; Shin *et al.*, 2004), and anodization (Ismail *et al.*, 2011a; Ismail *et al.*, 2011b; Mushove *et al.*, 2015; Tsuchiya *et al.*, 2005; Wang *et al.*, 2015). Here, the structures were grown from metal foil by anodization as illustrated in Figure 1.4.

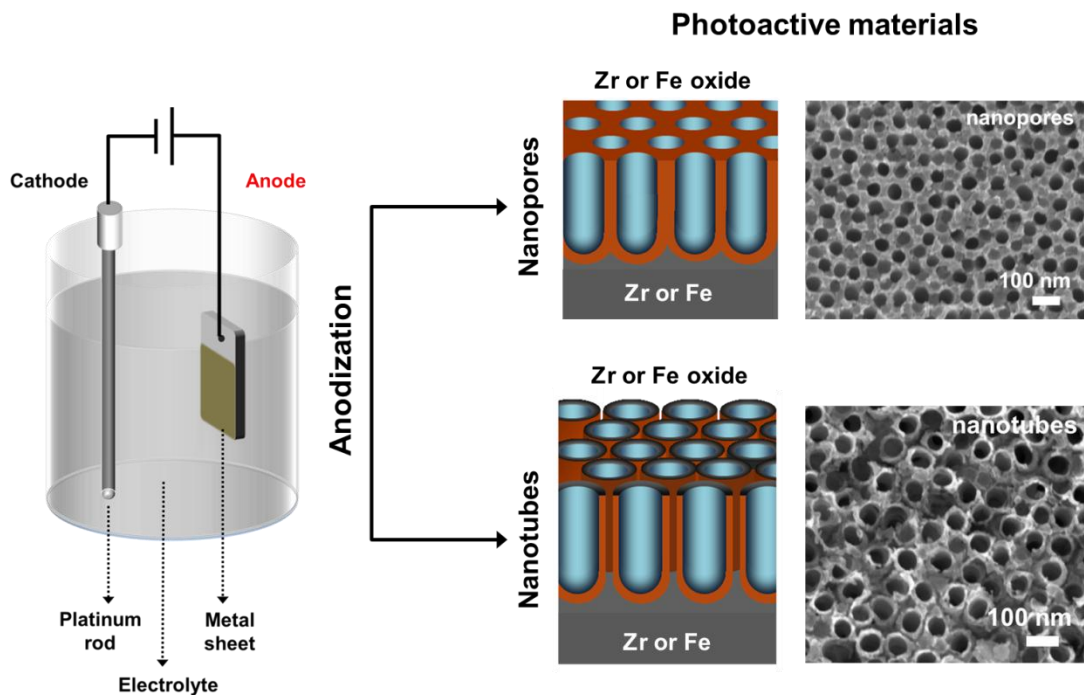


**Figure 1.4:** Schematic illustration for nanopores and nanotubes metal oxides formation by anodization as photoactive materials.

Anodization offers a simple, quick, and cost effective process of fabrication of elongated nanoporous and nanotubular metal oxides. As seen from Figure 1.4, it is

carried out typically in a cell containing suitable electrolyte, with metal foil of interest as anode and an inert platinum rod as cathode. Moreover as mentioned, the use of anodization process is unique since it can form a high temperature stable cubic or tetragonal  $ZrO_2$  phase (Habazaki *et al.*, 2000) without the need of intentional doping process. As will be discussed later, in this work anodization of Zr resulted in  $ZrO_2$  nanotubes (ZNTs) and on iron foil either  $\alpha$ - $Fe_2O_3$  nanopores (FNPs) or  $\alpha$ - $Fe_2O_3$  nanotubes (FNTs) can be produced (Figure 1.4).

As stated earlier,  $ZrO_2$  has a wide bandgap 3 – 6 eV which means that EHPs generation only can happen under UV light irradiation. For the case of  $TiO_2$ , metal dopants have been used to produce energy levels or states above the valence band and oxygen vacancies near the conduction band (Nakamura *et al.*, 2000). These new energy levels narrows the bandgap. For example electron can be excited to the oxygen vacancy states under visible light (Kim *et al.*, 2016) as shown in Figure 1.5. Adopting this idea, defective ZNTs were produced hence it can be visible light active. Formation of oxygen vacancies was introduced by anodization process and the presence of  $K^+$ ,  $Li^+$  or  $F^-$  in the electrolyte may induce unintentionally doping during nanotubes synthesis process.

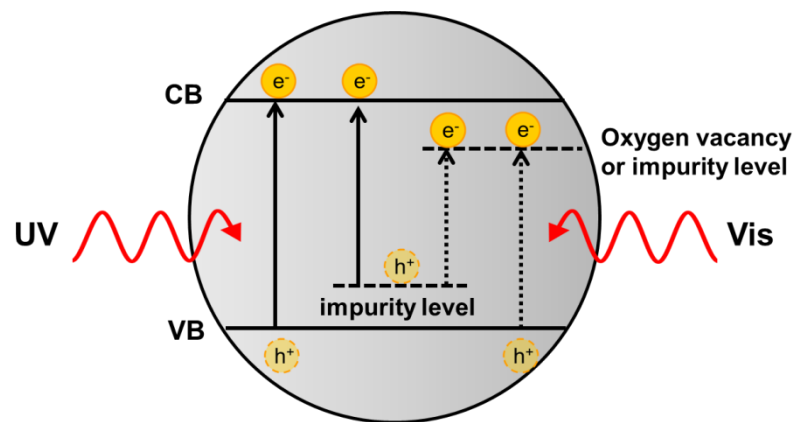


**Figure 1.5:** Band gap modification of photoactive oxide semiconductors by oxygen vacancies or impurities (where VB and CB is valence band and conduction band respectively).

#### 1.4. Problem statements

This study was aimed at the formation of ZNTs and FNPs/FNTs by anodization to be used as photoactive materials: photoanode for photocurrent generation and photocatalyst for water purification from dye contamination. Limited studies exist for both on the formation of ZNTs and FNPs/FNTs by anodization and their applications as photoactive materials as most published works are on the well-known material: TiO<sub>2</sub> (Grimes and Mor, 2009; Lee *et al.*, 2014b; Ochiai and Fujishima, 2012; Paramasivam *et al.*, 2012; Roy *et al.*, 2011). The rationale of using both ZrO<sub>2</sub> and  $\alpha$ -Fe<sub>2</sub>O<sub>3</sub> is that their band gap energies are sufficient for promoting a wide range of chemical reactions of environmental interest. However there are several material related challenges needed to be overcome: (1) minimizing recombination, (2) utilization of solar spectrum for catalyst activation, and (3) formation of crystalline oxide as the as-made oxides are amorphous which limits their applications.

In a thin compact film, the direction of light absorption is the same across the film with photogenerated carriers transfer from the surface and the bulk of the film to the back contact (Walter *et al.*, 2010) to give photocurrent (Figure 1.6(a)). The distance of holes can diffuse before recombination (or holes diffusion length) must be larger than  $1/\alpha$  (where  $\alpha$  is absorption coefficient of semiconductor near bandgap) in order to reduce recombination. Nevertheless, oxide semiconductor have small hole diffusion coefficient making them easily recombine with electrons. In order to overcome the holes diffusion problem, the semiconductor needs to be as thin as possible. But in a compact film, the film must be thick enough to absorb significant light that can be converted into useful EHPs. Instead of compact film, nanostructuring of the oxide film is believed to enable the creation of thicker oxide film but with much reduce recombination problem. Nanostructuring can be done by

creating thin film comprising of perfect arrays of nanotubes or nanopores. As seen in Figure 1.6(c), nanotubes have thin walls hence once created; the holes must only travel at a shorter distance to reach the surface. If the walls can be made much smaller than the mean free path and the diffusion coefficient of the holes, the carriers are thought to be able to move with minimum resistance and recombination.

It is well known that film with nanostructures have higher surface area than compact film. This will allow larger area for absorption of light. Nanopores also have thin walls, but their walls are not separated (Figure 1.6(b)) whereas nanotubes have well separated pore cells (discrete), and hence light absorption and EHPs formation are thought to be more efficient (Figure 1.6(c)). Moreover, the as mentioned, distance travelled of carriers from the pore walls to the side for transfer process will be much reduced as well. By utilizing nanostructured film, harvesting light from the source is thought to be much improved translating to higher density of electrons and holes in the surface of the catalysts. Therefore, in this thesis anodic method to produce oxide films comprising of either nanotubes or nanopores structure were explored in great depth.

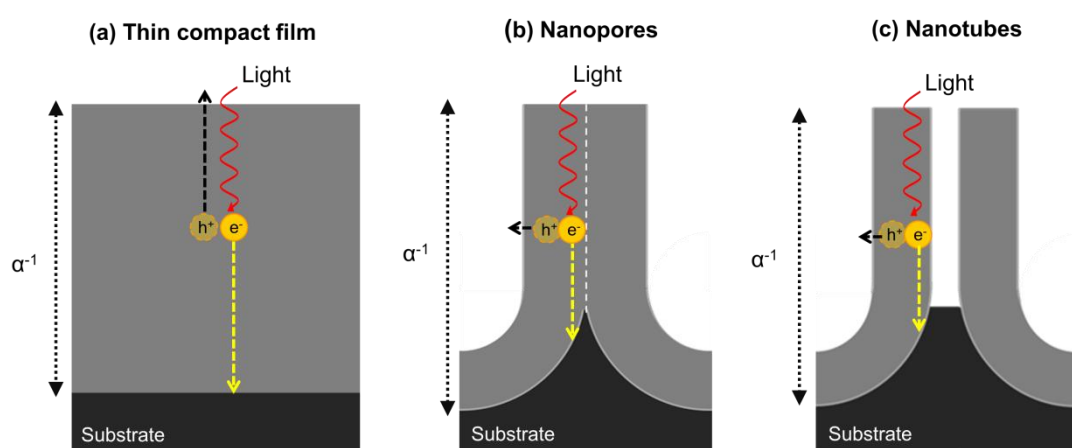


**Figure 1.6:** In a thin compact film (a), photogenerated carriers must traverse the entire thickness of the film,  $\alpha^{-1}$  (where  $\alpha$  is the absorption coefficient), before collection. In a nanopores film (b) and nanotube-array film (c), carriers must only reach the nanotube surface before recombination.

The peak of solar spectrum (AM 1.5) is at a greenish wavelength of 502 nm within the visible region (Bak *et al.*, 2002; Tsui and Zangari, 2014). On the shorter wavelength side, the spectrum extends to the visible purple range and falls sharply within the ultraviolet (UV) region. On the longer wavelength side, the spectrum extends much more into the infrared region (Zhu and Yu, 2016). A solar spectrum is therefore consisted of UV light (< 400 nm), visible light (400 – 700 nm), and infrared regions (> 700 nm). In order to harvest the visible part of the spectrum, photoactive materials used must have energy gap within the energy of visible light photons. Second generation photoactive materials can be classified as semiconductors that have greater absorption of light in visible region (Emeline *et al.*, 2012). Wide band gap semiconductor like ZrO<sub>2</sub> is not suitable to be used under visible light. However in this thesis ZNTs were made rather defective, hence it can be activated under visible part of the solar spectrum. To achieve defective ZNTs, various metal ions impurities like F<sup>-</sup>, K<sup>+</sup>, and Li<sup>+</sup> and oxygen vacancies were introduced. O<sup>2-</sup> and hydroxyl ion (OH<sup>-</sup>) are needed for oxide formation, but with the field effect ionic migration process occurring during anodic process, the anodic ZNTs tend to have defects especially oxygen vacancies. The existence of such defect can narrow down the energy gap of the oxide. On the other hand, α-Fe<sub>2</sub>O<sub>3</sub> is an intrinsically narrow gap semiconductor whereby the oxide can be activated readily under visible part of the solar spectrum. The oxide has however problem related to short hole diffusion length.

In EG electrolyte, H<sub>2</sub>O has been vastly used as an O<sup>2-</sup> and/or OH<sup>-</sup> provider (Lee *et al.*, 2014a; Schrebler *et al.*, 2014; Wang *et al.*, 2015). But instead of H<sub>2</sub>O, the addition of KOH into EG electrolyte has been proposed as oxygen provider (oxidant) to produce TiO<sub>2</sub> nanotubes (TNTs) (Krengvirat *et al.*, 2013; Nyein *et al.*, 2017; Taib

*et al.*, 2017).  $K^+$  was also shown to be inserted into TNTs and resulting high photoactivity (Krengvirat *et al.*, 2013).  $K^+$  added TNTs required applied bias lower than that pure TNTs for photocurrent generation (Richter *et al.*, 2009; Richter and Menon, 2010). In addition, hydroxyl group ( $OH^-$ ) was found on the surface of TNTs produced in KOH/ $NH_4F$ /EG electrolyte and surface  $OH^-$  affects the photoactivity performance whereby they can trap holes at the lattice oxygen atoms to form OH radicals ( $OH^\bullet$ ) (Taib *et al.*, 2017). Similarly,  $Li^+$  insertion to TNTs was reported to enhance photocurrent and PEC efficiency (Kang and Park, 2013; Meekins and Kamat, 2009). In addition, LiOH and  $H_2O_2$  can be used as an  $O^{2-}$  and/or  $OH^-$  provider in EG electrolyte to induce faster growth rate and aspect ratio TNTs (Joseph and Sagayaraj, 2015; Lin *et al.*, 2008; Raj and Prasanth, 2015; Raj *et al.*, 2015; Sreekantan *et al.*, 2011; Wang *et al.*, 2011). As to date, despite various works reported on TNTs, there is no report on the effect of the addition of these different  $O^{2-}$  and/or  $OH^-$  providers into EG electrolyte on morphology, crystallinity, optical property and photoactivity performance of both ZNTs and FNPs/FNTs. This thesis reports on the characteristics of ZNTs and FNPs/FNTs formed by anodization process in KOH, LiOH or  $H_2O_2$  added  $NH_4F$ /EG electrolyte. Experiments were done to build further understanding on how the ZNTs produced in various  $O^{2-}$  and/or  $OH^-$  providers behave as photocatalyst or as photoanode in PEC cell under UV and visible light irradiation. The photoactive properties of FNPs/FNTs produced in EG added with various  $O^{2-}$  and/or  $OH^-$  providers were also studied by measuring photocurrent or dye degradation (photocatalytic experiments) under visible light irradiation.

Another challenge associated with anodic ZNTs and FNPs/FNTs are that they are amorphous (Ismail *et al.*, 2011a; Stępień *et al.*, 2014; Zhao *et al.*, 2008). The amorphous structure limits their application as photoactive materials as amorphosity

reduce chances for EHPs formation and promotes recombination. Amorphous structure also demonstrates the lack of stability in a solution of low pH level (Stępień *et al.*, 2014) and hence when used in liquid (as in when immersed in solution for photocatalytic process), the oxide tends to be dissolving or absorbing significant amount of water. In order to convert the amorphous into crystalline structure, annealing is required. Nevertheless, annealing may also induce grain growth and sintering, thus destroying the nanotubular or nanoporous structure. As the optical and electronic properties of annealed ZNTs have not been thoroughly explored, it is the intention here to report on detailed analysis on what happened when these oxides were annealed. Morphologies of the oxides were viewed as a function of annealing temperatures. The photoactivities of the annealed oxides were then studied. It was later observed that the substrate material also oxidized during the course of annealing

It was realized that Zr foil is rather expensive and hence recycling of the substrate material is preferred. In one part of this thesis, a study on the formation of freestanding ZNTs (FS-ZNTs) – the film detached from the foil is reported. There are more advantages of the use of FS-ZNTs, for instance by utilizing FS-ZNTs, the influence of the substrate can be eliminated during annealing. It is also of interest to have liquid penetrating inside the interior of the nanotubes for more oxide-liquid interaction, therefore by using FS-ZNTs, both sides of the film can be used as oppose to when it is fixed on the Zr. In this thesis, ZNTs were formed in  $\text{H}_2\text{O}_2/\text{NH}_4\text{F}/\text{EG}$  electrolyte as to weaken the adherence of the oxide film to the Zr hence FS-ZNTs were produced. To the best of knowledge, the use of this method has not been reported in current literature and thus there were various parameters studied and reported in this thesis. Similar to the other samples, photocatalytic properties of FS-ZNTs were also assessed.

### 1.5. Research objectives

The main objectives of this thesis are:

1. To study the formation of ZNTs on the Zr and FNPs/FNTs on Fe by anodization in  $\text{NH}_4\text{F}/\text{EG}$  electrolyte added with varying  $\text{O}^{2-}$  and/or  $\text{OH}^-$  provider
2. To investigate the influence of annealing on ZNTs and FNPs/FNTs to their morphology, crystallinity, and property
3. To elucidate FS-ZNTs formation by anodic process
4. To assess the photoactivity performance (as photocatalysts for dye degradation or as photoanode for photocurrent generation in a PEC cell) of ZNTs/FS-ZNTs and FNPs/FNTs under visible light irradiation.

### 1.6. Research scope

In this research work, three main aspects to discuss are the formation of ZNTs and FNPs in various  $\text{O}^{2-}$  and/or  $\text{OH}^-$  providers, characterization, and performance evaluation as photoactive materials. The scope of this research covered:

1. Anodization process was done only with EG as the bulk electrolyte added to it  $\text{NH}_4\text{F}$  and different  $\text{O}^{2-}$  and/or  $\text{OH}^-$  providers added ( $\text{H}_2\text{O}$ ,  $\text{KOH}$ ,  $\text{LiOH}$ , and  $\text{H}_2\text{O}_2$ ). Aqueous electrolyte and other organic electrolyte were not studied.
2. ZNTs and FNPs/FNTs formed by anodization were characterized by Field Emission Scanning Electron Microscopy (FESEM), Transmission Electron Microscopy (TEM), High Resolution Transmission Electron Microscopy (HRTEM), Energy Filtered Transmission Electron Microscopy (EFTEM), Electron Spectroscopic Imaging (ESI), X-ray Diffraction (XRD), Raman spectroscopy, X-ray Photoelectron Spectroscopy (XPS), Fourier Transform



Infrared (FTIR) spectrometer, Ultraviolet-visible spectrophotometry (UV-Vis), and Photoluminescence (PL) spectral measurements only.

3. Photoactive material performance was studied by measuring photocurrent in a simple PEC cell utilizing NaOH as electrolyte. No other electrolyte or another more complex system was studied. Photocatalytic process was done by measuring the reduction of concentration in organic dye under light illumination. No other experiments were done.

### **1.7. Thesis outline**

The thesis is consisted of five chapters. Chapter 1 is the overall introduction for the whole thesis. Chapter 2 presents the literature review of the anodization process in  $\text{NH}_4\text{F}/\text{EG}$  electrolyte and mechanism of nanopores and nanotube formation. The literature review of application of ZNTs and FNPs/FNTs as photoactive materials is presented in that chapter as well. Chapter 3 deals with the material, chemicals used, and experimental procedure of this study. Chapter 4 focuses on presenting the overall results and discussion on formation of ZNTs and FNPs/FNTs, their properties and photoactivity performance. Chapter 5 is on the conclusion and suggestions for further studies on this work.

## **CHAPTER TWO**

### **LITERATURE REVIEW**

#### **2.1. Introduction**

This chapter emphasizes on three main parts. First part reviews the anodization process for nanostructuring. The second part reviews the anodization of Zr metal for ZrO<sub>2</sub> nanotubes (ZNTs) formation which includes: (1) progress in Zr metal anodization in various types of electrolyte until the discovery of ZNTs, (2) growth mechanism model and factors affecting the growth of ZNTs, (3) methods to form freestanding ZNTs, (4) crystallinity and phase stabilization, and (5) properties and photoactivity of ZNTs. The last part reviews the anodization of Fe metal for  $\alpha$ -Fe<sub>2</sub>O<sub>3</sub> nanopores/nanotubes (FNPs/FNTs) formation and their photocurrent generation.

#### **2.2. Anodization process for nanostructuring**

Anodic oxidation or anodization of metals has been used to protect metal components from corrosion and for decorative purposes for more than 10 decades (Aladjem, 1973). However, anodization has become a technique not only for protection or to increase the aesthetic appearance of the metal components but explicitly done to produce a thin oxide film. Anodic thin oxide film on a metal has many unique properties leading to various interesting applications. For instance anodizing aluminum (Al) resulted in Al<sub>2</sub>O<sub>3</sub> film which has raised substantial scientific and technological interest in recent years due to the dielectric property of the oxide which can be used in electrolytic capacitors (Ban *et al.*, 2014). Anodized titanium (Ti) on the other hand has been widely investigated as the TiO<sub>2</sub> film

produced, being a photoactive semiconductor has many applications especially in the field of solar energy utilization (Grimes and Mor, 2009; Kowalski *et al.*, 2013; Sauvage *et al.*, 2010). TiO<sub>2</sub> is also a well-known photocatalysts hence anodizing Ti can be used to produce TiO<sub>2</sub> photocatalyst that can degrade organic pollutants in contaminated air and water (Ao and Lee, 2005; Lee and Park, 2013; Sreekantan *et al.*, 2009).

As mentioned, anodization is a process that resulted in the formation of thin oxide film on a metal substrate. When a metal (M) is exposed to a sufficiently high anodic applied voltage in an oxidizing electrolyte, an oxidation reaction will take place. Generally the reaction can be written as Equation 2.1:



If the metal ions, M<sup>n+</sup> are solvated in the electrolyte, no anodic film will form and the metal will continuously dissolve. Depending on the rate of dissolution, the metal components can be completely corroded or only a thin layer will be removed as a typical process in electropolishing of metal. If the electrolyte is comprised of oxidant species that can react with the solvated ions, then a metal oxide (MO) can be formed (Equation 2.2).



Now the properties of MO will determine the fate of the underlying metal. If the MO is easily dissolved then the metal will not be protected. If the MO is not dissolving, a barrier layer is formed and such a compact film may protect the underlying metal from further corrosion. Normally this can be achieved at relatively low anodizing voltage and by an appropriate choice of electrolyte. A competition between solvatization and oxide formation can also be observed whereby the anodic

film will dissolve but at the same time oxidized to form MO. Therefore, depending on the electrolyte used, the surface oxide formed on anodized metal can either be compact or porous. Porous film can be further classified as a film consisted of random pores, ordered pores or pores formed by loosely bounded small particulates on the metal surface forming a three dimensional network of interconnected particles.

Ordered pores can be in a form of discreet pores, characterized by elongated holes forming perpendicular to the underlying metal substrate. The pores can be of micron of depth but the diameter is normally less than 100 nm hence they are termed nanopores. An anodic oxide film with such morphology is called nanoporous oxide. Anodizing Al in acidic electrolyte is a well-known example whereby the resulting anodic Al<sub>2</sub>O<sub>3</sub> is consisted of such nanopores (Sulka, 2008). Moreover, not only the nanopores formed are elongated, forming channels of equal diameter and length, the channels are actually highly densely packed in hexagonal arrangements. The first work reported on this observation is by Masuda and Fukuda whereby they mentioned that under specific experimental conditions pores growth is highly organized (Masuda and Fukuda, 1995). Applications of such structure are endless and one of it is as a template to produce nanowires or nanotubes. The use of nanoporous Al<sub>2</sub>O<sub>3</sub> or termed anodic aluminium oxide (AAO) as a template for synthesis of 1-D nanomaterials is reported by Uosaki et al. (Uosaki *et al.*, 1990). Following this pioneering work, many reports have appeared on the use of AAO as 1-D nanostructures template material. The AAO pores are filled with the desired material; metal, polymer or semiconductors, then the AAO template will be etched away to yield nanorods or nanotubes.

Anodic process to yield self-organized pores on other metals such as W (Ismail *et al.*, 2016; Ng *et al.*, 2015), Nb (Kim *et al.*, 2016; Stojadinović *et al.*, 2015), Ti (Dikici *et al.*, 2017; Lee, 2017; Toshiaki *et al.*, 2016), Zr (Amer *et al.*, 2014; Berger *et al.*, 2008b; Wierzbicka *et al.*, 2016), and Fe (Cheng *et al.*, 2012b; Konno *et al.*, 2012; Wang *et al.*, 2015) and semiconductors like Si (Kim *et al.*, 2004) and InP (Li *et al.*, 2016; Sato *et al.*, 2006) have then received more attention. In the early works, focus was given on the formation of anodic oxide with similar morphology: close-packed cells in a hexagonal arrangement with nanopores at their centers. Optimization of the process to have control over pore diameter and length has been done. Anodization voltage has a strong influence the diameter and length of the nanopores formed. When the morphology of the AAO is inspected further, the pore cell is found to consist of scalloped shaped bottom. This is readily observed especially when the oxide layer is removed from the metallic substrate; exploring this allows for the proposal of several mechanistic models that describe the occurrence of the self-organized AAO.

The mechanisms of formation have then been adopted to explain the development of similar structure on other metals examples as mentioned earlier. Among the metals (and semiconductors) stated, Ti has been the most studied considering the anodic layer (i.e. TiO<sub>2</sub>) possesses many excellent properties for applications in environment remedy and energy production as stated before (Chen and Mao, 2007; Mor *et al.*, 2006). Work published by Zwilling *et al.* can be regarded as the first report on the formation of self-organized TiO<sub>2</sub> nanostructure by anodic process (Zwilling *et al.*, 1999). In the said work chromic acid electrolyte containing hydrofluoric acid was used to form what appears to be nanotubular structure. Despite the poor wall appearance, this work presents the most significant findings

such that fluoride ions are needed in the electrolyte to allow the transformation of nanopores to nanotubes. Following this, more reports have emerged on the formation of oxide nanotubes especially  $\text{TiO}_2$  with fluoride ions as the main ingredient in the electrolyte that allows for pores to tubes transformation (Wang *et al.*, 2009; Wang and Lin, 2009).

There are four main components in the process of anodization: metal foil, platinum, power supply and electrolyte. The electrolyte can be consisted of fluoride ions ( $\text{F}^-$ ), oxygen ions ( $\text{O}^{2-}$ ) and hydroxide ions ( $\text{OH}^-$ ) in viscous electrolyte. The positively charged electrode is the anode where the oxidation reaction occurs and the negatively charged electrode is the cathode where reduction reaction is dominating. When the anode is metal (and platinum as cathode), the applied voltage generates an electric field across the metal and causes the anodic film in form of barrier oxide layer to grow as  $\text{O}^{2-}$  ions migrate inward under the influence of the electric field and the metal ions eject out from the metal. Anodic film has different volume than the parent metal, thus it is expected to be under compressive stress. Following the flow concept for the growth of porous anodic  $\text{Al}_2\text{O}_3$  (Houser and Hebert, 2009), oxide flow is assumed to originate from the plasticity of the barrier oxide layer generated by compressive stresses. To minimize stress the oxide behaves viscoplastically and it is continually being pushed upwards from the metal|oxide interface forming scalloped structure which will then develop into pores. The transition from pores to tubes structures can occur by dissolving interpores boundaries which is consisted of fluoride-rich layer. This layer is soluble in water, hence sufficient amount of water is needed to dissolve it and then tube can be produced.

### **2.3. Anodization of Zr metal for ZNTs formation**

This section reviews the history of Zr anodization in various electrolytes to form  $ZrO_2$  compact oxide layer, nanopores, or nanotubes. There has been a significant progress made regarding the synthesis of ZNTs which has led to: first generation ZNTs prepared in aqueous electrolyte containing NaF or  $NH_4F$ , second generation ZNTs grown in hydrofluoric acid (HF), third generation smooth ZNTs in organic electrolyte and finally fourth generation ZNTs in fluoride free electrolyte. This thesis focuses on ZNTs formed in organic electrolyte, specifically in ethylene glycol containing  $NH_4F$  and various types of oxidant. Growth mechanism model and factor affecting the growth of ZNTs in organic electrolyte, the phases of  $ZrO_2$  and stabilization of certain phases, properties and photoactivity of ZNTs are reviewed here.

#### **2.3.1. Progress in Zr metal anodization in various types of electrolyte**

Cox in 1970 anodized Zr to form a compact oxide layer of up to several hundred nanometers thickness. The Zr metal was first etched in mixed nitric/hydrofluoric acid then anodized in aqueous electrolyte (Cox, 1970).  $F^-$  ions in ammonium borate electrolyte was used to anodize Zr as reported by Archibald and Leach (Archibald and Leach, 1977a; Archibald and Leach, 1977b) to produce compact  $ZrO_2$  as well. In 1988, Khalil et al. reported on the anodization of Zr in various aqueous electrolytes and showed the formation of hydrated layer on the oxide surface (Khalil *et al.*, 1988).